FORTH
Institute of Electronic Structure and Laser

Imaging and quantification of lipid stores in adipose and muscular tissue in *Caenorhabditis elegans* samples via nonlinear microscopy.

Barbara Petanidou

Department of Physics

University of Crete

July 2016

Master Thesis

SUPERVISOR: Prof. Costas Fotakis

Co-Supervisors: Dr. George Filippidis

Dr. Meropi Mari

Τριμελής Επιτροπή

Κώστας Φωτάκης: Καθηγητής στο Τμήμα Φυσικής Πανεπιστημίου Κρήτης

Νεκτάριος Ταβερναράκης: Καθηγητής στο Τμήμα Ιατρικής Πανεπιστημίου Κρήτης

Ειρήνη Αθανασάκη : Καθηγήτρια στο Τμήμα Βιολογίας Πανεπιστημίου Κρήτης

Ευχαριστίες

Η παρούσα μεταπτυχιακή διατριβή εκπονήθηκε στο Ινστιτούτο Ηλεκτρονικής Δομής και Λέιζερ (ΙΗΔΛ-IESL) του Ιδρύματος Τεχνολογίας και Έρευνας (ITE-FORTH) και αποτελεί αποτέλεσμα συνεργασίας του εργαστηρίου της Μη Γραμμικής Μικροσκοπίας (ΙΗΔΛ-IESL) και του εργαστηρίου του Καθ. Νεκτάριου Ταβερναράκη στο Ινστιτούτο Μοριακής Βιολογίας και Βιοτεχνολογίας (IMBB).

Πρωτίστως, θα ήθελα να ευχαριστήσω θερμά τον επιβλέπων καθηγητή μου κ.Κώστα Φωτάκη για την δυνατότητα που μου παρείχε να εργαστώ στο άρτια εξοπλισμένο και ιδιαίτερα φιλικό και φιλόξενο ερευνητικό περιβάλλον του Ιδρύματος Τεχνολογίας και Έρευνας, καθώς και για την γενικότερη επίβλεψη της εργασίας.

Στη συνέχεια, θα ήθελα να απευθύνω τις ευχαριστίες μου στον επιβλέποντα ερευνητή Δρ. Γιώργο Φιλιππίδη για την συνεχή καθοδήγηση και επίβλεψή του στο πειραματικό μέρος , στην ανάλυση των αποτελεσμάτων αλλά και για την συνεχή ενθάρρυνση και εμπιστοσύνη του κατά τη διάρκεια της μεταπτυχιακής διατριβής, καθότι αποτέλεσε και τυπικά ο υπεύθυνος της πειραματικής διαδικασίας.

Τέλος, ιδιαίτερες ευχαριστίες θέλω να απευθύνω στους μεταδιδακτορικούς ερευνητές και φίλους Μερόπη Μαρή και Γιώργο Τσερεβελάκη για όλες τις συνθήκες εργασίας από την αρχή έως το τελικό στάδιο ολοκλήρωσης των πειραματικών διαδικασιών, για την παροχή όλης της προηγούμενης και πολύτιμης εμπειρίας και τεχνογνωσίας τόσο σε θεωρητικό όσο και σε πρακτικό επίπεδο εφαρμογής της καθώς και για την υπομονή και επιμονή την οποία επέδειξαν.

Επιπρόσθετα, θα ήθελα να ευχαριστήσω την μεταδιδακτορική ερευνήτρια Ευγενία Μεγάλου και τον υποψήφιο διδάκτορα Κώστα Παλικαρά οι οποίοι εργάζονταν στον εργαστήριο του Καθ. Νεκτάριου Ταβερναράκη στο Ινστιτούτο Μοριακής Βιολογίας και Βιοτεχνολογίας (IMBB) για την προετοιμασία των βιολογικών δειγμάτων και επεξήγηση εννοιών και προβλημάτων της βιολογίας που προέκυψαν κατά τη διάρκεια της εργασίας.

Table of content

Chapter 7. Imaging and quantifying ectopic fat accumulation in muscular region of *C. elegans*.

Περίληψη

Η διερεύνηση των μοριακών μηχανισμών που ρυθμίζουν την αποθήκευση λιπιδίων και το μεταβολισμό τους μέσω μή καταστρεπτικών απεικονιστικών τεχνικών μπορεί να παρέχει πολύτιμες πληροφορίες για την πρόληψη της παχυσαρκίας η οποία έχει συσχετιστει με μια σειρά πολύ σοβαρών παθολογικών καταστάσεων όπως καρδιαγγειακές διαταραχές και διαβήτης τύπου ΙΙ.

Στη παρούσα μεταπτυχιακή διατριβή το νηματοειδές σκουλήκι Caenorhabditis elegans (C. elegans) χρησιμοποιήθηκε ως οργανισμός μοντέλο. Με τη πραγματοποίηση μη γραμμικών απεικονιστικών μετρήσεων γένεσης δεύτερης και τρίτης αρμονικής συχνότητας (SHG, THG) και πολυφωτονικά διεγειρόμενου φθορισμού (MPEF) κατέστη δυνατή για πρώτη φορά η λεπτομερής καταγραφή της μορφολογίας, των δομών και των λιπιδικών εναποθέσεων του δείγματος σε μικροσκοπικό επίπεδο.

Με τη χρήση αυτών των μη καταστρεπτικών τεχνικών πραγματοποιήθηκε η παρακολούθηση της συγκέντρωσης λιπιδίων σε λιπώδεις και μη λιπώδεις ιστούς στις περιοχές του εντέρου και του φάρυγγα αντίστοιχα, αγρίου τύπου και μεταλλαγμένων, μη σημασμένων ζώων. Μέσω της ποσοτικοποίησης των συλλεγόμενων μη γραμμικών σημάτων γένεσης τρίτης αρμονικής συχνότητας (THG) επετεύχθη η συσχέτιση της συσσώρευσης λιπιδικών εναποθέσεων με την γήρανση του δείγματος. Δείχτηκε ότι υπήρξε μια σημαντική αύξηση των λιπιδίων στη περιοχή του εντέρου (adipose fat) κατά τη διάρκεια της ανάπτυξης του σκουληκιού, η οποία ακολουθείται από μια βαθμιαία μείωση κατά τη διάρκεια της ενήλικης του ζωής. Επιπλέον, ανιχνεύτηκε αύξηση των λιπιδικών εναποθέσεων στη περιοχή του φάρυγγα (ectopic fat) κατά την διάρκεια της γήρανσης των βιολογικών δειγμάτων .

Τα αποτελέσματα που προέκυψαν αποδίδουν χρήσιμες και πολύτιμες πληροφορίες για τη συσχέτιση της διαδικασίας της γήρανσης και της λιποτοξικότητας στον οργανισμό μοντέλο C. elegans. Επιπρόσθετα καταδεικνύουν τις μη γραμμικές απεικονιστικές τεχνικές και κυρίως τη γένεσης τρίτης αρμονικής συχνότητας ως καινοτόμα, γρήγορα, αξιόπιστα, μη επεμβατικά εργαλεία στην έρευνα για τη βιολογία των λιπιδίων.

Abstract

The investigation of molecular mechanisms that regulate lipid storage and its metabolism through non-destructive imaging techniques can provide valuable and significant information for preventing obesity that is related with a sequence of very serious pathological situations such as cardiovascular disorders and diabetes type II.

In current study, nematode Caenorhabditis elegans (*C. elegans*) has been used as a model organism. The accomplishment of non-linear imaging measurements of second (SHG), third harmonic (THG) generation and multiphoton fluorescence (MPEF) provided for the first time in details the morphology, structure and lipid depositions in samples at microscopic level.

By employing these non-destructive techniques, imaging and monitoring the lipid accumulation has been achieved in adipose and non-adipose (ectopic fat) tissue in the region of intestine and pharynx respectively in non labelled wild type and mutant animals. The quantification of the collected non-linear signals of third harmonic generation reveals the correlation between lipid depositions and aging of the sample. It was also shown that a significant increase in lipids in the intestine region (adipose fat) during developmental stages of *C. elegans* followed by a decrease during its adult lifespan. Moreover, it has been detected an increase of lipid depositions in the pharynx region (ectopic fat) during aging of the biological samples.

These results could afford remarkable and profound information for the relation between aging process and lipotoxicity in the model organism *C. elegans*. Additionally, they prove that third harmonic generation can act as a novel, reliable fast and non-invasive tool for providing new insights in lipid biology research.

Introduction

Femtosecond lasers constitute an excitation light source with high intensities that are useful for nonlinear phenomena such as Two Photon Fluorescence (TPEF) and Second (SHG) and Third (THG) Harmonic Generation. Moreover they introduce new diagnostic tool which basic principle are tightly focused femtosecond pulses (10^{-15}sec) and the density of photons is high enough to originate multiphoton absorption or other nonlinear process. Several dyes with maximum peak in ultraviolet (UV) or visible (VIS) region of the electromagnetic spectrum can be excited by two or three infrared (IR) photons. Nonlinear absorption and fluorescence are taken place in the focal plane of the laser beam with succeed in high resolution and furthermore the 3D imaging of the examined biological sample. Previous imaging techniques suffer from low physical or chemical specificity such as conventional microscopy in combination with fluorescence or Raman spectroscopy. Their spatial resolution is restricted by the diffraction limit imposed by the wavelength of the probe light. Conventional microscopy also does not provide microscopic information about the real surface structure of the sample.

Nonlinear optical measurements used in conjuction with microscopy observation have created new chances in imaging techniques. Second-order nonlinear processes such as second-harmonic generation (SHG), third-order processes such as third-harmonic generation (THG), coherent anti-Stokes Raman scattering (CARS), and two-photon excited fluorescence (TPEF) have been used for the imaging, monitoring and further understanding of biological systems and processes. *In our work images and results obtained by using the nonlinear processes of the TPEF , THG and SHG which will be presented*.

Two photons, typically in the infrared spectral range, have energies approximately equal to half of the energetic difference between the ground and excited electronic states. Since the two-photon excitation probability is significantly less than the one-photon probability, two-photon excitation occurs with appreciable rates only in regions of high temporal and spatial photon concentration. The high spatial concentration of photons can be achieved by focusing the laser beam with a high numerical aperture (NA) objective lens to a diffraction-limited focus. The ability to limit the region of excitation is very important, especially for biological specimen, since their photodamage is restricted only to the focal point. Since out-of-plane fluorophores are not excited, they are not subject to photobleaching. Moreover, TPEF microscopy exhibits an additional advantage. Two-photon excitation wavelengths are red-shifted to approximately twice the one-photon excitation wavelengths. The significantly lower absorption and scattering coefficients ensure deeper tissue penetration.

In SHG and THG, light of the fundamental frequency ω is converted by the nonlinear material into light at exactly twice that frequency, 2ω and 3ω. The discovery that exogenous markers can lead to exceptionally high signal levels has been a leading cause for the revival of SHG

microscopy. In particular, SHG markers, when properly designed and collectively organized, can produce signal levels easily comparable to those encounterd in standard TPEF microscopy. Many intrinsic structures of biological systems produce strong SHG signal, so labeling with exogenous molecular probes is not always required. SHG signal is produced from non-centrosymmetric molecules and provides information, which is related to structures with high degree of orientation and organization but without inversion symmetry. TPEF relies on nonlinear absorption, followed by fluorescence emission, and hence is not a coherent process. In contrast, SHG relies on nonlinear scattering, and hence is a coherent process. SHG such as TPEF exhibits intrinsic three-dimensionality and ability to section deep within a biological tissue, due to its nonlinear nature. It has a significant efficiency only at extremely high incident light intensities, and therefore arises only from a well-defined volume around the focal center of the incident light beam. Moreover, in SHG imaging technique, like in TPEF, the wavelength of the fundamental incident light lies in the IR spectum region, thus suffering less from scattering and absorption inside the biological samples and exhibiting large penetration depths. SHG is a second-order nonlinear phenomenon, and its strength is fully determined by the second-order susceptibility tensor $\chi^{(2)}$ of the nonlinear medium.

In THG microscopy, third harmonic light is generated at the focal point of a tightly focused ultra-short pulsed laser beam. Due to the coherent nature of the THG, no net signal is obtained when focussed inside a homogeneous, normally dispersive medium. This is because of the Gouy phase shift experienced by the excitation beam near the focus. However, when the nonlinear medium is not uniform, either in the refractive index or in the nonlinear susceptibility, the THG signal does not vanish, but significant THG signal can be obtained. This coherent nature of the THG process enables THG microscopy highly sensitive to in-homogeneities and the efficiency of signal generation strongly depends on the relative size of the in-homogeneity and the focal volume. This specificity makes THG microscopy useful as a tool for material characterization.

In our work nonlinear techniques SHG, THG and TPEF implemented in *Caenorhabditis elegans* (*C. elegans*) in order to study functional responses of the *C. elegans* with aging processes. The nematode *C. elegans* is characterized of optical transparency which makes it an ideal model for application of either optical microscopy or laser based techniques. It is the first animal to have its entire genome sequenced and its nervous system has been reconstructed with electron microscopy. Many parts of the animal such as neurons or lipid accumulation have been found to contribute to specific functions. The coordinated function of lipids leads to characteristic behavioral responses, many diseases and aging processes.

By using the strong diagnostic tool of THG we start our study to identify and localize lipid content in adipose tissue of the intestine region in *C. elegans.* Lipid deposition of the animal erupt many optical properties, interfaces or optical eterogeneities in comparison with the size of the focused laser beam. We excluded the possibility that lipofuscin contributes to the THG signal and instead found that fat is the main contributor of high THG signal in the intestine of *C.*

Elegans. To ensure our approach, it was shown that multiphoton excitation fluorescence, following lipid staining with BodiPy 500/510, Nile Red and Oil Red-O and THG signals were colocalized in wild type worms. The basic adipose tissue in *C. elegans* was found in the intestine region and imaging lipid deposition necessitate THG as a reliable and with great significance tool that monitors lipid accumulation. Afterwards, we used THG microscopy for imaging and monitoring lipid accumulation in non-adipose tissue (ectopic fat accumulation). The selected non-adipose tissue region is the pharyngeal muscles. The simultaneous application of THG and SHG let us oversee the lipid content (THG) on the muscular region of *C. elegans* (SHG). The musculature of the animal is set in the region of pharynx where the anatomical information for the muscular structure was obtained by SHG. Measurements were taken place in several samples of wild type and mutant animals in different developmental stages for the purpose of ensure the initial assessment.

For the evaluation and processing our results we used MatLab algorithm based on the selected THG signal through which we monitor lipid depositions. The information that we got was the surface area of ectopic lipid content in the muscular region of *C.elegans* (Non Adipose Fat) and also in the region of intestine (Adipose Fat). Quantification of the examined area has been achieved that correlates lipid deposition with aging. Via this study it was shown tha THG is a powerful, new, reliable diagnostic tool for lipid biology research.

Chapter 1. Optical Harmonics Generation

1.1 Non Linear Optical Processes

Nonlinear optical processes can be observed when high electric field strength is implemented to a medium. Therefore they occur when the response of a material system to an applied optical depends in a nonlinear manner on the strength of the optical field. This kind of electric field is afforded often by intense laser light and it is necessary for demonstrating many nonlinear effects such as *Second and Third Harmonic Generation, Multiphoton Fluorescence*, in the optical frequency range.

As light, and so laser light, is an electromagnetic wave, consists an electric and a magnetic field component. Specifically, the electric field component is responsible for many interactions with matter. The propagation of light (propagation of the electric field) is described by a wave equation, derived from the Maxwell's equation of the electromagnetic field which in vacuum is expressed as:

$$\nabla^2 \vec{E} - \frac{1}{c^2}\frac{\partial^2 \vec{E}}{\partial t^2} = 0 \qquad (1.1.1)$$

where $\vec{E}$ is the electric field component and ∇^2 is the Laplacian. In vacuum the phase velocity c is known as $c = \frac{1}{\sqrt{\mu_0 \varepsilon_0}}$ where μ_0 is the vacuum permeability and ε_0 is the vacuum permittivity respectively.

Linear light interaction

Here the electric field strength of light gives us a harmonic wave as solution:

$$\vec{E}(\vec{r},t) = \vec{A}\exp\left[i(\vec{k}\cdot\vec{r} - \omega\cdot t)\right] + c.c. = \vec{E}_0 \exp(-i\omega t) + c.c. \qquad (1.1.2)$$

where $\vec{A}$ is the wave amplitude and $\left(\vec{k}\cdot\vec{r} - \omega\cdot t\right)$ is its phase, $\vec{r}$ is the position vector and t is the time. The propagation vector $\vec{k}$ has magnitude in vacuum:

$$\left|\vec{k}\right| = k = \frac{2\pi}{\lambda} = \frac{\omega}{c} \qquad (1.1.3)$$

where λ is the wavelength and ω is the angular velocity given by ω = 2πv.

In a general way, when an electric field is applied on a medium, it polarizes its molecules and rouses dipole momentum $\vec{\mu} = e\vec{d}$, where e is the electronic charge and $\vec{d}$ is the relevant displacement.

The macroscopic equivalent of the dipole moment is the polarization P:

$$\vec{P} = Ne\vec{d} \qquad (1.1.4)$$

where N is the number of dipoles per unit volume.

Polarization $\vec{P}$ or dipole moment per unit volume of a material system depends on the strength $\vec{E}(t)$ of an applied optical field. At lower excitation intensities due to weak electric field, the optical response of a medium is linear and the polarization is linearly proportional to the electric field. This can be described by the relationship:

$$\vec{P} = \varepsilon_0 \chi^{(1)} \vec{E}(t) \qquad (1.1.5)$$

where $\chi^{(1)}$ is the constant of the proportionality and is known as the linear susceptibility or first order electric susceptibility ,given by a second rank tensor and ε_0 is the permittivity of free space.

Nonlinear light interaction

Contrary to linear way, in a nonlinear manner, the optical response can be described by expressing the polarization $\vec{P}$ (t) as a power series in the field strength $\vec{E}(t)$ as:

$$\vec{P}(t) = \varepsilon_0 \left[\chi^{(1)} \vec{E}(t) + \chi^{(2)} \vec{E}^2(t) + \chi^{(3)} \vec{E}^3(t) + \ldots \right] \equiv \vec{P}^{(1)} + \vec{P}^{(2)} + \vec{P}^{(3)} + \ldots \qquad (1.1.6)$$

The quantities $\chi^{(2)}$ and $\chi^{(3)}$ represent the second and third – order nonlinear electric susceptibility, given by a second and third rank tensor respectively. Purposely, when the electric field originates from a harmonic light wave, which is formed as:

$$\vec{E} = E_0 \sin \omega t \qquad (1.1.7)$$

the equation (1.1.6) becomes:

$$\vec{P}(t)=\varepsilon_0\left[\chi^{(1)}E_0\sin\omega t+\frac{\chi^{(2)}E_0^2}{2}(1-\cos 2\omega t)+\frac{\chi^{(3)}E_0^3}{4}(3\sin\omega t-\sin 3\omega t)+\ldots\right] \quad (1.1.8)$$

The above equation (1.1.8) has a great importance, because is composed of an infinite sum of oscillating terms with angular frequencies that are integer multiples of ω, which reveals that nonlinear susceptibilities depend on the frequencies of the applied fields. Also, it is remarkable to mention that polarization at time t depends only on the instantaneous value of the electric field strength.

Each term gives us special information. For example, the first term, $\chi^{(1)}E_0\sin\omega t$ constitutes the linear response of the medium in the applied time-varying field. The second term $\frac{\chi^{(2)}E_0^2}{2}(1-\cos\omega t)$ is consisted of two components. The first one represents a constant quantity which depends on the square of the field amplitude. In this case, an effect known as optical rectification is observed, which is a result of a constant bias electric polarization of the material. The second one reveals a dependence on the $\cos 2\omega t$ function. This is a time-varying change of the electric polarization at an angular frequency which is the double fundamental field frequency, in other words a part of the re-radiated light due to the accelerated electrons has double frequency. As a result, second harmonic irradiation is generated. The third term of the equation $\frac{\chi^{(3)}E_0^3}{4}(3\sin\omega t-\sin 3\omega t)$ shows that the polarization contains a component which oscillates at an angular frequency 3ω and it is responsible for the re-radiation of the incident field energy as third harmonic generation light.

1.2 Linear and nonlinear assumption of susceptibility

While nonlinearity has electronic origin, the linear and nonlinear susceptibilities lead to harmonics generation procedure. The linear relationship between polarization and electric field (1.1.5) exists when the medium is electrically linear or isotropic. The optical properties of a medium are expressed by the real and imaginary parts of the dielectric constant, ε_r, which is derived from the polarization $\vec{P}$ of the medium:

$$\vec{D} = \varepsilon_0 \vec{E} + \vec{P} = \varepsilon_0 \varepsilon_r \vec{E} \qquad (1.2.1)$$

Since the relative electric permittivity ε and the refractive index n are related through the expression

$$n^2 \approx \varepsilon_r \qquad (1.2.2)$$

the linear susceptibility $\chi^{(1)}$ is connected to ε through the combination of equation (1.1.5) and (1.2.1) and results:

$$\varepsilon_r = 1 + \chi^{(1)} \qquad (1.2.3)$$

Consequently, we see that the $\chi^{(1)}$ is in the order of unity. At this point, it is clear that when the light intensity is small, the refractive index is independent of the applied electric field, hence of the intensity $I \propto |E|^2$. Though, since $\chi^{(1)}$ is a second-rank tensor, the index can depend on the polarization of the wave.

When the amplitude of the applied field is of the same order of the characteristic atomic field strength $E_{atomic} = 5.14 \cdot 10^{11} V/m$ for the hydrogen atom, it is expected that the lowest order correction term in the general expression of the electric polarization to be comparable to the linear response. Thus,

$$\chi^{(1)} E_{atomic} \approx \chi^{(2)} E_{atomic}^2 \qquad (1.2.4)$$

and since $\chi^{(1)}$ is of the order of unity, we find that the second order susceptibility is approximately equal to $1/E_{atomic}$, or that

$$\chi^{(2)} \approx 1.94 \cdot 10^{-12} m/V \qquad (1.2.5)$$

Additionally, $\chi^{(3)}$ is expected to be of the order of $1/E^2{}_{atomic}$, hence

$$\chi^{(3)} \approx 3.78 \cdot 10^{-24} m^2/V^2 \qquad (1.2.6)$$

In nonlinear optics we need to consider the consequence of a changing electric susceptibility as it varies with the strength of the electric field of the light. The relationship between $\vec{P}$ and

$\vec{E}$ could be generalized as the summation of a first order response and series of nonlinear terms with an increasing order:

$$\begin{aligned}\vec{P} &= \vec{P}^{L} + \vec{P}^{NL} \\ \vec{P} &= \vec{P}^{(1)} + \vec{P}^{(2)} + \vec{P}^{(3)} + ...\vec{P}^{(N)} \\ P &= \varepsilon_0 (\chi^{(1)} E + \chi^{(2)} E \cdot E + \chi^{(3)} E \cdot E \cdot E + ...\chi^{(N)} E^{N})\end{aligned} \tag{1.2.7}$$

So, the nonlinear relationship between polarization and electric field appears only with strong fields. Therefore, the light intensity I is related with the electric field as follows:

$$I = 2n\left(\frac{\varepsilon_0}{\mu_0}\right)^{1/2} \left|\vec{E}_0\right|^2 \tag{1.2.8}$$

Let us now assume that total polarization field consists of the first and the third order and it oscillates at frequency ω and the electric field E is given by:

$$E = E_\omega \cos \omega t \tag{1.2.9}$$

where E_ω is the amplitude of the wave. Subsequently, combining the equation (1.2.7) and taking only the linear terms and those in the third order we get a polarization:

$$P \approx \varepsilon_0 (\chi^{(1)} + \chi^{(3)} \left|E_\omega\right|^2) E_\omega \cos \omega t \tag{1.2.10}$$

Since, we have (1.2.2), the refractive index gets a nonlinear character:

$$\begin{aligned} n &\approx n_0 (1 + \frac{1}{2{n_0}^2} \chi^{(3)} \left|E_\omega\right|^2) \\ n &= n_0 + n_2 I \end{aligned} \tag{1.2.11}$$

where n_0 is the linear refractive index , n_2 is the nonlinear refractive index and I is the intensity of the wave.

The linear susceptibility is much greater than the nonlinear susceptibilities $\chi^{(3)} \left|E_\omega\right|^2 << {n_0}^2$. Hence, optical nonlinearities are only noticeable at high-amplitude fields. This means that the material response to the incident fields of weak to moderate intensities will be linear and contrary to them, with larger fields the higher-order terms in the Taylor expansion become significant as the response of the electrons inside the medium becomes nonlinear.

For that reason, all the optical properties of a material and the corresponding phenomena, such as absorption, emission, refraction, reflection and scattering, are accounted for by the susceptibility.

1.3 Wave equation of Nonlinear Optical Interaction

At this point we demonstrate the use of Maxwell's equation in order to describe how electromagnetic radiation interacts with matter.

While polarization is acting with electromagnetic field, it generates new frequency components. For example let's consider a radiation field that oscillates at ω_1 and ω_2 frequencies. It is also propagating along z axis. Now, the electric field is described by:

$$E(t) = A_1 \cos(\omega_1 \cdot t + k_1 z) + A_2 \cos(\omega_2 \cdot t + k_2 z) \qquad (1.3.1)$$

and the nonlinear polarization $\vec{P}^{(2)} = \chi^{(2)} \vec{E} \cdot \vec{E}$ depends on the square of the electric field. The square of (1.3.1) at z=0 is:

$$E^2(t) = A_1^2 \cos^2(\omega_1 \cdot t) + A_2^2 \cos^2(\omega_2 \cdot t) + 2A_1 A_2 \cos(\omega_1 \cdot t)\cos(\omega_2 \cdot t) \qquad (1.3.2)$$

which becomes under some trigonometric identities:

$$E^2(t) = \frac{1}{2}(A_1^2 + A_2^2) + \frac{1}{2} A_1^2 \cos(2\omega_1 \cdot t) + \frac{1}{2} A_2^2 \cos(2\omega_2 \cdot t) + A_1 A_2 \{\cos\cdot[(\omega_1 + \omega_2)\cdot t] + \cos\cdot[(\omega_1 - \omega_2)\cdot t]\}$$

We can easily notice that this kind of field contains a time independent, two terms that oscillate at the double frequency $2\omega_1$ and $2\omega_2$, also a term oscillating in sum-frequency $\omega_1 + \omega_2$ (*sum frequency generation – SGF*). This process is also used to convert a weak light signal from ω_1 to ω_3 by mixing it with a laser beam at ω_3. At the difference frequency $|\omega_1 - \omega_2|$ (*difference frequency generation DFG*) and is used to generate coherent light in the infrared by mixing two laser beams at close frequencies. The process where a polarization at zero frequency is obtained , is called *optical rectification (OR)*.

The phenomenon of SHG is illustrated by using energy – level diagrams, involving ''virtual'' transitions. (Figure 1.3.1)

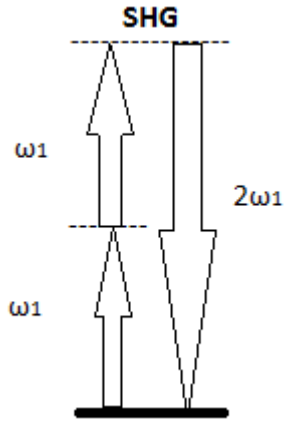

Figure 1.3.1: Energy level diagram for a simple picture of second harmonic generation.

All frequencies require some well-defined conditions, the phase-matching conditions so, they are not produced simultaneously. Each frequency gives us a special phenomenon which we will discuss in later chapter.

The propagation of light through a nonlinear optical medium can be determined by wave equation, derived from Maxwell's equation:

Faraday's law $$\vec{\nabla} \times \vec{E} = -\frac{\partial \vec{\mathbf{B}}}{\partial t} \qquad (1.3.3)$$

Gauss's law for electric field $$\vec{\nabla} \cdot \vec{E} = \frac{\rho}{\varepsilon_0} \qquad (1.3.4)$$

Gauss's law for magnetic field $$\vec{\nabla} \cdot \vec{B} = 0 \qquad (1.3.5)$$

Ampere's law $$\vec{\nabla} \times \vec{B} = \mu_0 \left(\vec{J} + \varepsilon_0 \frac{\partial \vec{E}}{\partial t} \right) \qquad (1.3.6)$$

where ε_0 is the vacuum permittivity , μ_0 is the magnetic permeability , $\rho(r,t)$ is the density of free charges and $\vec{J}(r,t)$ the corresponding current density of free charges. These equations give solution in regions of space that contain no free charges, so that

$$\vec{\rho} = 0 \qquad (1.3.7)$$

and no free currents, so that

$$\vec{J} = 0 \qquad (1.3.8)$$

As the material is assumed to be nonmagnetic, the magnetic field is given by:

$$\vec{B} = \mu_0 \vec{H} \qquad (1.3.9)$$

In the next step, we derive the optical wave equation. Firstly, we take the curl of the curl $\vec{E}$ Maxwell equation of Faraday's law (1.3.3):

$$\vec{\nabla} \times \left(\vec{\nabla} \times \vec{E}\right) = -\frac{\partial\left(\vec{\nabla} \times \vec{B}\right)}{\partial t} \qquad (1.3.10)$$

Afterwards, we get the curl of both sides of (1.3.9) and we substitute the Ampere law from (1.3.6) to derive

$$\vec{\nabla} \times \vec{B} = \mu_0 \frac{\partial \vec{D}}{\partial t} \qquad (1.3.11)$$

By substituting the (1.3.11) into (1.3.10) we end up with the wave equation for propagation in a polarized material

$$\vec{\nabla} \times \vec{\nabla} \times \vec{E} + \mu_0 \frac{\partial^2 \vec{D}}{\partial t^2} = 0 \qquad (1.3.12)$$

We have to notice that the fields $\vec{D}$ and $\vec{E}$ are related by (1.2.1). Because of this the polarization vector $\vec{P}$ has a nonlinear dependence on the applied field $\vec{E}$. Thus, by combining (1.3.12) with (1.2.1) we get the equation

$$\vec{\nabla} \times \vec{\nabla} \times \vec{E} + \frac{1}{c^2} \frac{\partial^2 \vec{E}}{\partial t^2} = -\mu_0 \frac{\partial^2 \vec{P}}{\partial t^2} \qquad (1.3.13)$$

where the component of the electric field of the incident radiation is related to the electric polarization of the material. This expression is the most general form of the wave equation in nonlinear optics. For simplicity, the first term of (1.3.13) can be written as follows:

$$\vec{\nabla} \times \vec{\nabla} \times \vec{E} = \vec{\nabla}(\vec{\nabla} \cdot \vec{E}) - \vec{\nabla}^2 \vec{E} \qquad (1.3.14)$$

Due to the linear, isotropic and source free medium, the first term of the right hand side of (1.3.13) does not exist and since (1.2.1) and (1.3.4) imply that

$$\vec{\nabla} \cdot \vec{E} = 0 \qquad (1.3.15)$$

Consequently, (1.3.13) becomes

$$\vec{\nabla}\times\vec{\nabla}\times\vec{E}\approx-\vec{\nabla}^2\vec{E} \qquad (1.3.16)$$

If we substitute (1.3.16) into (1.3.13) we have a simplest form

$$\vec{\nabla}^2\vec{E}-\frac{1}{c^2}\frac{\partial^2\vec{E}}{\partial t^2}=\mu_0\frac{\partial^2\vec{P}}{\partial t^2} \qquad (1.3.17)$$

For the case of an isotropic and dispersionless material (ε_r is considered to be frequency independent), we can combine both (1.3.17), (1.2.3) and (1.2.7)

$$\vec{\nabla}^2\cdot\vec{E}-\frac{n^2}{c^2}\frac{\partial^2\vec{E}}{\partial t^2}=\mu_0\frac{\partial^2\vec{P}^{Nl}}{\partial t^2} \qquad (1.3.18)$$

Where n is the linear refractive index (1.2.2) and $c^2=\frac{1}{\mu_0\varepsilon_0}$.

Equation (1.3.18) represents the nonlinear response of a medium, which becomes a source terms as we see from the right-hand side. In the absence of that term, (1.3.18) represents an equation of a free wave propagating with phase velocity c/n. As we will see in the next chapter, the second – order time derivative of the non – linear part of the electric polarization is responsible for the harmonics generation within the medium.

1.4 Higher Harmonic Generation

Second Harmonic Generation (SHG)

As it was discussed in Chapter 1.1, second harmonic generation (SHG) appears in the second term of (1.1.8) and it reveals a dependence on the $\cos 2\omega t$ function. This is a time-varying change of the electric polarization at an angular frequency which is the double fundamental field frequency, in other words a part of the re-radiated light due to the accelerated electrons has double frequency. As a result, second harmonic irradiation is generated.

This phenomenon arises from a mixing of applied frequencies in a non-linear medium. Since the nature of the polarization field is dependent on the incident electric fields, the effects resulting from the non-linear susceptibilities are denoted by the appropriate order susceptibility, incident and resultant electric field frequencies. Equation (1.2.7) can be written as:

$$P_i=\chi_{ij}^{(1)}E_j+\chi_{ijk}^{(2)}E_jE_k+\chi_{ijkl}^{(3)}E_jE_kE_l \qquad (1.4.1)$$

The first coefficient $\chi_{ij}^{(1)}$ is the linear electric susceptibility and is given by a second rank tensor. The second coefficient $\chi_{ijk}^{(2)}$ is called second order susceptibility, given by a third rank tensor. In case of second harmonic generation we consider the interaction of an optical electric field at frequency ω and amplitude E_ω, it emerges:

$$E_\omega(t) = E_\omega(e^{+i\omega t} + e^{-i\omega t}) \tag{1.4.2}$$

with a static electric field E_0 in a medium with non-zero $\chi^{(2)}$. So, the second-order polarization field in this medium from (1.2.7) is:

$$\begin{aligned}\vec{P}^{(2)}(t) &= \chi^{(2)}\vec{E}^2(t) \\ &= \chi^{(2)}\left[E_\omega e^{+i\omega t} + E_\omega e^{-i\omega t} + E_0\right]^2 \\ &= \chi^{(2)}\left[E_\omega^2(e^{+i2\omega t} + e^{-i2\omega t}) + 2E_0E_\omega(e^{+i\omega t} + e^{-i\omega t}) + 2E_\omega^2 + E_0^2\right]\end{aligned} \tag{1.4.3}$$

The polarization field that results contains components oscillating at various frequencies. The first term in (1.4.3) oscillates at 2ω and radiates light at that frequency. This term depends only on the presence of the filed at frequency ω and not on the static field, referred to as second harmonic generation (SHG). The second term oscillates at ω and causes a variation in the refractive index in the medium. This effect , is known as electro-optic effect. The third and last term does not oscillate in time and it is known as optical rectification.

For the second order susceptibility, equation (1.4.1) can be rewritten as:

$$P_i^{(2)} = \chi_{ijk}^{(2)}(-\omega_3;\omega_1,\omega_2)E_j^{\omega_1}E_k^{\omega_2} \tag{1.4.4}$$

where indices *i, j, k* denote Cartesians components of the electric fields oscillating at $\omega_3, \omega_2, \omega_1$, respectively. The frequencies are related such that:

$$\omega_3 = (\omega_1 + \omega_2) \tag{1.4.5}$$

where ω_3 is the output frequency, ω_1 and ω_2 are the frequencies of the incident electric fields. Some of the effects characterized by the second order susceptibility are:

$\chi_{ijk}^{(2)}(-2\omega;\omega;\omega)$	Second Harmonic Generation (SHG)
$\chi_{ijk}^{(2)}(-\omega_1-\omega_2;\omega_1;\omega_2)$	Sum Frequency Generation (SFG)
$\chi_{ijk}^{(2)}(-\omega_1+\omega_2;\omega_1;\omega_2)$	Difference Frequency Generation (DFG)

Since Second Harmonic Generation is a second order nonlinear phenomenon, occurs when the medium is a non-centrosymmetric material and arises through an interaction between the electric field and the its spatial derivative. The emission by this process is coherent, highly anisotropic and phase-coupled to the excitation. Therefore, phase-matching effects between electric waves are necessary. Another main process for scattering photons at twice the excitation frequency is Hyper-Rayleigh Scattering (HRS), referring the dephased re-emission of one photon after two excitation photons have been absorbed. It is spontaneous, isotropic and the absorption and re-emission depends on the dipole included in the medium by nonlinear interaction with the incident field. The harmonic signal that is generated due to the randomness of the phases will be relatively weak and incoherent and its propagation will be in every possible spatial direction. On the other hand, when the dipole population has orientation in space, the HRS phenomenon results into coherent harmonic generation procedure under strong phase-matching conditions .

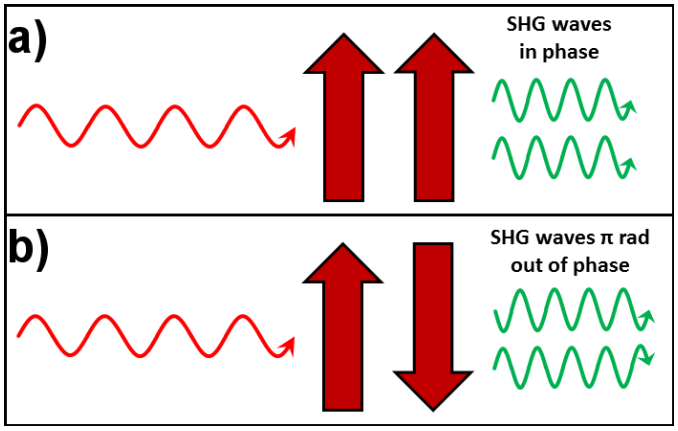

Figure 1.4.1: a) *The two dipoles oscillate in phase and the generated second harmonic waves are added constructively to form a well-defined beam,* b) *Totally destructive interference occurs and SHG vanishes for a π rad phase difference.*

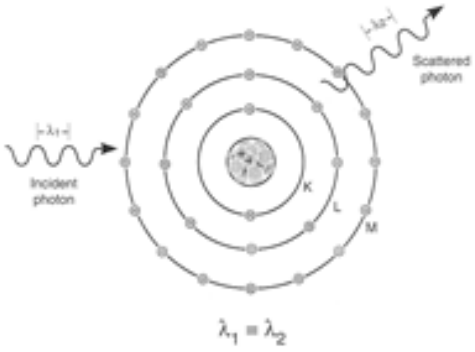

Figure 1.4.2: *Configuration of the incident photon that interacts with and excites the total atom as opposed to individual electrons.*

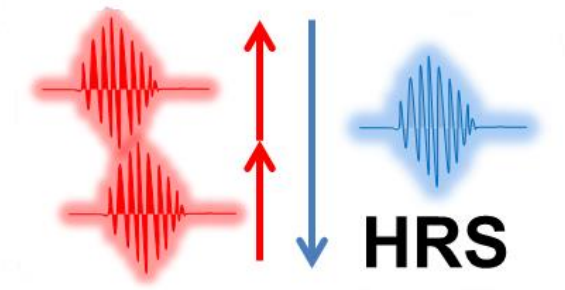

Figure 1.4.3*: Hyper Rayleigh scattering (HRS) where two photons scatter at twice the excitation frequency.*

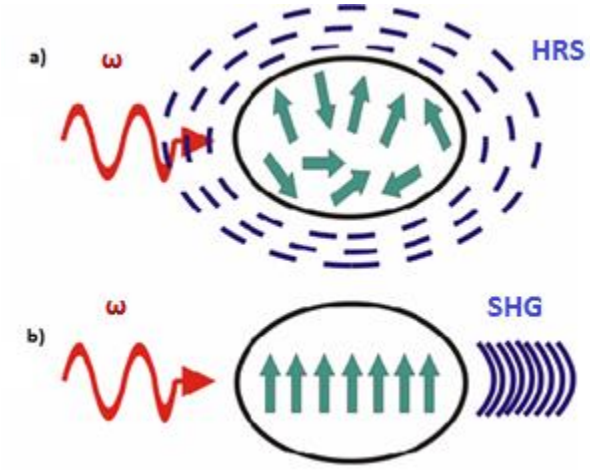

Figure 1.4.4*: a) Dipoles are oscillating in random directions in HRS, therefore the generated direction at 2ω is weak, non-directional and incoherent. b) In SHG case the dipoles have some orientation in space and SHG irradiation will occur as a result of the constructive interference of the individually generated waves.*

For real case, there is a requirement on materials properties so the second order nonlinear optical processes can occur with a significant efficiency only if a standard phase matching condition is satisfied. In plane wave the condition which describes it mathematically is:

$$\Delta k = k_3 - k_2 - k_1 \qquad (1.4.6)$$

Here, k_3 is the wave vector of the highest frequency wave and k_1, k_2 are those of other waves. The efficiency of SHG is maximized when a positive phase mismatch Δk ($\Delta k = 0$) and $n(\omega) = n(2\omega)$ is introduced, providing perfect phase matching conditions. Because of the frequency dependence (dispersion) of the refractive index, the phase matching condition is often satisfied by using birefringence, the dependence of the refractive index on the polarization of the incident light, presented by several materials. As far as SHG microscopy is concerned, the most common biological structures that present the necessary conditions (non-centrosymmetric molecules and birefringence) for the effective generation of second harmonic signal are collagen, myosin fibrils, tubulin, etc.

Third Harmonic Generation (THG)

Contrarily to Second Harmonic Generation (SHG), Third Harmonic Generation (THG) is third order phenomenon which can appear in every kind of material, centrosymmetric and not. The third order response leads to processes such as third harmonic generation and two-photon absorption. More importantly, leads to the intensity dependent refractive index. The intensity dependence of refractive index described by (1.2.11) .

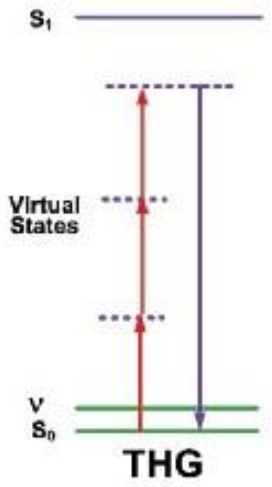

Figure 1.4.5: *Energy level diagram of THG where is depictured S_0 and S_1, ground and first excited singlet states.*

Third order nonlinearity arises from expanding the nonlinear susceptibility to third order in the electric field, as it was described in (1.1.8) and it shows that the polarization contains a component which oscillates at an angular frequency 3ω and it is responsible for the re-radiation of the incident field energy as third harmonic generation light. From the equation (1.4.1) we see the coefficient $\chi_{ijk}^{(3)}$ which is called third order susceptibility.

The third order polarization induced by the focused fields is described by:

$$P_i^{(3)} = \chi_{ijkl}^{(3)}(-3\omega_3;\omega_1,\omega_2,\omega_3)E_j^{\omega_1}E_k^{\omega_2}E_l^{\omega_3} \qquad (1.4.7)$$

Now there are three electric fields, E_0 that oscillates at ω_0, E_2 oscillating at ω_2 and E_3 oscillating at ω_3.

Third harmonic can be considered, depending on the medium, as being generated by three fundamental photons requiring phase matching and its nonlinear refractive index which depends quadratically on the light's electric field is written as (1.2.11). At this point we notice that n_2 is related to $\chi^{(3)}$. This coefficient consists of two parts, the real and imaginary part and the imaginary susceptibility leads only to nonlinear (absorption) effects. The real one leads to scattering effects. It is also related to one- , two-, or three- photon absorption:

$$\chi^{(3)}(\omega_4,\omega_3,\omega_2,\omega_1) \approx n(\omega_4)n(\omega_3)\,n(\omega_2)n(\omega_1) \qquad (1.4.8)$$

So that, $\chi^{(3)} \approx n(3\omega)\,n(\omega)^3$.

Alternatively, the nonlinear refractive index can be calculated by Kramers–Kronig relation, which relates the nonlinear refractive index to the spectrum of nonlinear absorption, assuming the same level of excitation. The Kramers-Kronig relation states that when optical intensity I is present at a frequency ν, a change in refractive index Δn can be determined by measuring the change in absorption at all possible frequencies ν', under the same excitation conditions and integrating by means of the following equation:

$$\Delta n(\nu) = \frac{c}{2\pi^2} P\int_0^\infty \frac{\Delta\alpha(\nu')}{\nu'^2 - \nu^2} d\nu' \qquad (1.4.9)$$

Chapter References

1. R.L. Sutherland, *Handbook of Nonlinear Optics*, Marcel Dekker Inc., New York (1996).

2. R.W. Boyd, *Nonlinear Optics (Third Edition)*, Academic Press, Burlington, MA (2008).

3. M. Born and E. Wolf, *Principles of Optics (Seventh Edition)*, Cambridge Univ. Press, New York (2011).

4. F. Trager (Ed.), *Springer Handbook of Lasers and Optics*, Springer Science + Business Media, New York (2007).

5. Y.R. Shen, *The Principles of Nonlinear Optics*, Wiley, New York (1984).

6. B.R. Masters and P.T.C. So (Ed.), *Handbook of Biomedical Nonlinear Optical Microscopy*, Oxford Univ. Press, New York (2008).

7. E. Hecht, *Optics (Fourth Edition)*, Addison Wesley, San Francisco (2002).

Chapter 2. Fluorescence

2.1 Theory of single photon absorption

Fluorescence is the emission of a photon and the electronic transition from the first excited singlet state to the singlet ground state after optical excitation. The energy of the emitted photon corresponds to the energy difference between the lowest vibrational level of the excited state and the vibrational level of the singlet ground state. Phosphorescence is the emission of a photon and the electronic transition from the first excited triplet state to the singlet ground state after optical excitation. These radiative transitions are called electric dipole transitions.

The electronic states in the diagram are characterized as either singlet or triplet. Typically singlet states are denoted with the symbol S_n and triplet states with the symbol T_n, where the letter n = 0, 1, 2, . . . represents the first, second, or higher electronic states. An understanding of singlet and triplet states requires first the introduction of a quantum property of subatomic particles called "spin". Spin is an intrinsic property of atoms, an "intrinsic rotation" of subatomic particles and generating magnetic moments either parallel or antiparallel to the magnetic field. Spin can have two possible states with magnitudes of $\pm\frac{h}{2\pi}$. As a shorthand, these states are referred to as spin $\frac{1}{2}$ or spin-up state and spin $-\frac{1}{2}$ or spin-down state. Singlet and triplet states of an atom refer to the spin configurations of its electrons.

In a molecule, the electrons populate the orbital of the ground, singlet state in pairs; the two electrons in each orbital have opposite spins and thus the total electron spin is zero, which defines the state as a singlet state. The excited singlet state can have a single electron in each higher-energy orbital, but the two electrons still have opposite spins. In the excited triplet state, the lower orbitals have two paired electrons each, but not the higher-energy orbitals, which contain one electron each, and spins are parallel so the triplet state has a net spin of 1. The term "triplet state" refers to the three possible energy levels that correspond to that state.

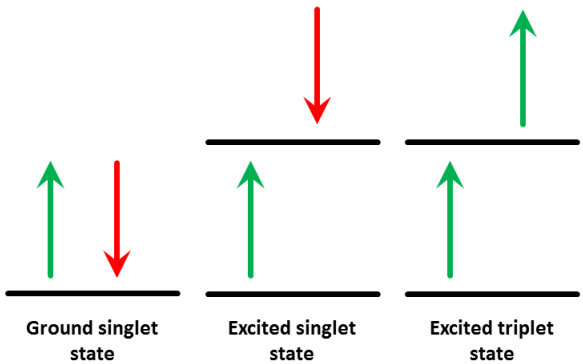

Figure 2.1.1: *Electron configuration for singlet and triplet states.*

In a classical view the electron has orbital angular momentum due to its motion around the nucleus. Since moving charges generate magnetic fields, the electron also has a magnetic moment associated with this orbital motion. There is also another magnetic moment due to the spin of the electron. Transitions between singlet–singlet and triplet–triplet are allowed, but transitions between singlet–triplet multiplicities and triplet–singlet are forbidden. Even these weak transitions between states of different multiplicities may be observed due to spin–orbit coupling, the interaction of spin and orbital magnetic moments of an electron.

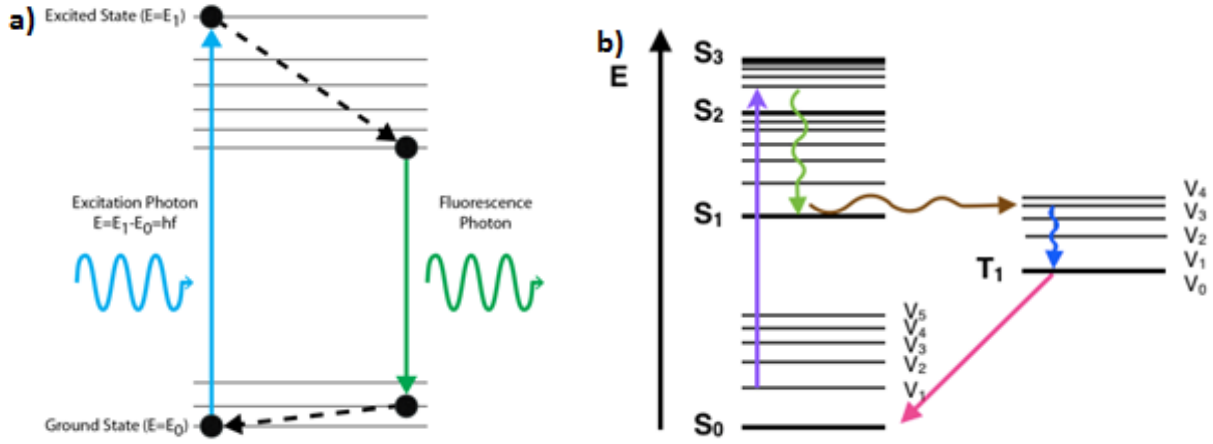

Figure 2.1.2: a) *Schematic transitions for one photon fluorescence.* **b)** *Schematic transitions for one photon fluorescence shown* ***absorbance*****,** ***internal conversion*****,** ***intersystem crossing*****,** ***vibrational relaxation*****,** ***phosphorescence.***

While a molecule can be excited to higher electronic states, the emission usually occurs from the lowest singlet state, S_1. Fluorescence is typically defined as the emission of photons accompanied by a $S_1 \rightarrow S_0$ relaxation, after optical excitation. There are rare cases of fluorescence occurring from higher excited singlet states. The fluorescence is composed of photons with an energy difference that corresponds to the lowest vibrational level of the excited singlet electronic state to the vibrational level of the ground state (Figure 2.1.2a). Therefore, the spectral properties of fluorescence do not depend on the excitation wavelength. A transition from the excited triplet state to the singlet ground state is "forbidden" and the rates are very slow; they are on the order of milliseconds to seconds. This process of electronic transitions from the first triplet electronic state to the various vibronic V_0, V_1, . . , V_4 energy levels of the singlet ground state, is called phosphorescence (Figure 2.1.2b).
One of the most important parameters of fluorescence is the lifetime because it determines the interval for the various dynamic processes that can affect the emission. The time ranges for the various processes determine the observed spectroscopic properties of a given molecule in a given environment (concentration, other molecules present, temperature, etc.). Absorption occurs in about 10^{-15} s. Intersystem crossing occurs in the range of 10^{-10} to 10^{-8} s. Internal conversion occurs in the range of 10^{-11} to 10^{-9} s. Vibrational relaxation occurs in the range of

10^{-12} to 10^{-10} s. The lifetime of the first excited singlet state is in the range of 10^{-10} to 10^{-7} s and occurs with the emission of fluorescence. The lifetime of the first excited triplet state T_1 occurs in the range of 10^{-6} to 1 s with the emission of phosphorescence.

2.2 Theory of multiphoton absorption

As absorption constitutes a strongly nonlinear process, is related to the imaginary part of the third order nonlinear susceptibility through (1.2.11). It depends quadratically on the incident intensity and it can be increased even in transparent media by introducing a multiphoton absorption at high intensity levels. Additionally, reduced absorption comes from saturating the absorption line with high intensity light. In a general way, absorption can be written as a function of intensity through:

$$\alpha(I) = \alpha_0 + \alpha_1 I + \alpha_2 I^2 \qquad (2.2.1)$$

where α_0 represents linear absorption, α_1 represents two-photon absorption, α_2 represents three-photon absorption, etc. This means that in multi-photon absorption the absorption increases with intensity. Even though a material is transparent at low intensity, as the intensity grows, the absorption may increase.

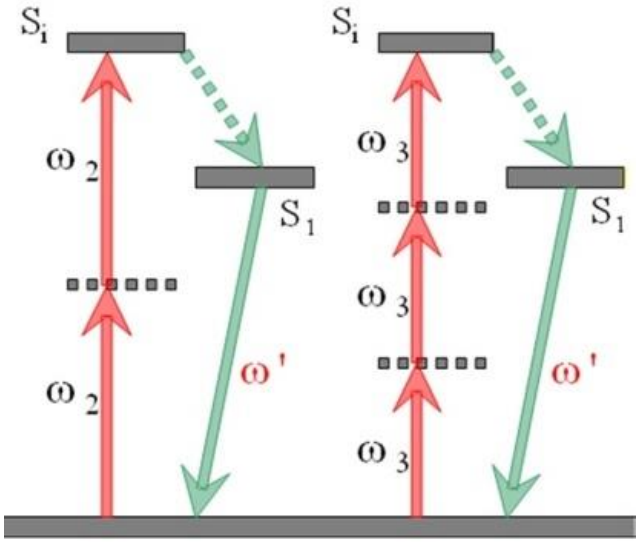

Figure2.2.1: *Configuration of multiphoton excited fluorescence*.

The simplest case of MPEF, *Two-photon absorption*, which may occur in transparent materials, can be large when the sum of two photon energies comes close an absorption resonance. This optical nonlinearity decreases the transmission of light as atoms or molecules absorb it while transitioning to higher levels. During TPEF, one photon having energy approximately equal to the half energy difference between the excited and the ground state interacts with the electron in order to excite it to an intermediate, quantum mechanically unobservable, virtual state where it will remain for an extremely small time. If the spatial and temporal density of the incident photons (i.e. the intensity of the radiation) is high enough, there is a finite probability that a second identical photon interacts with the electron which is found on the virtual state, so that the transition of the electron to the excited state to be achieved. As a result, the subsequent de-excitation of the electron back to the ground state will give a single fluorescence photon which constitutes the TPEF. There are two steps when TPEF is taking place. The first one refers to the absorption of a photon (or photons) so that an electron transition to the excited state is achieved and the second one to the de-excitation of the electron (usually back to the ground state) is taking place followed by the emission of one fluorescence photon.

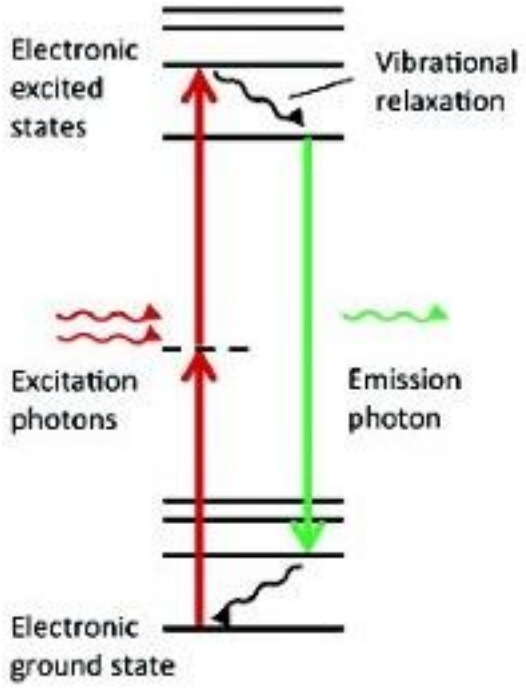

Figure 2.2.2: *Two photon fluorescence transition. Jablonski diagram showing the interaction of multiple infrared photons with the electronic and vibrational energy levels of a molecule. The molecule absorbs two infrared photons that promote it to the excited electronic state.*

From quantum mechanics point of view, the atomic wave function $\psi(r,t)$ obeys the time-dependent Schrodinger equation:

$$i\hbar\frac{\partial\psi(r,t)}{\partial t} = H\psi(r,t) \qquad (2.2.2)$$

where the Hamiltonian *H* is represented as

$$H = H_0 + V(t) \qquad (2.2.3)$$

Here H_0 is the Hamiltonian for a free atom and

$$V(t) = -\mu\vec{E}(t) \qquad (2.2.4)$$

$\mu = -er$ gives us the interaction energy with the applied optical field and as $E(t)$ we take the monochromatic wave of form:

$$E(t) = Ee^{-i\omega t} + c.c. \qquad (2.2.5)$$

which is switched suddenly at t=0.
Assuming that the solutions to Schrodinger's equation for a free atom are known, and that the wave functions associated with the energy eigenstates can be represented as:

$$\psi_n(\vec{r},t) = u_n(\vec{r})e^{-i\omega_n t} \qquad (2.2.6)$$

where $\omega_n = E_n/\hbar$ is the angular frequency.
The equation (2.2.6) is able to satisfy the (2.2.2) if u_n satisfies the eigenvalue equation:

$$H_0 u_n(\vec{r}) = E_n u_n(\vec{r}) \qquad (2.2.7)$$

When there is a time dependent interaction potential $V(t)$ Schrodinger's equation will take the form:

$$i\hbar\frac{\partial\psi(\vec{r},t)}{\partial t} = (H_0 + V(t))\psi(\vec{r},t) \qquad (2.2.8)$$

The solution of (2.2.8) can be expressed as a linear combination of the free atom H_0 eigenstates as:

$$\psi(\vec{r},t)=\sum_l \alpha_l(t)u_l(\vec{r})e^{-i\omega_l t} \qquad (2.2.9)$$

At this point, if we introduce (2.2.9) into (2.2.8) we get:

$$i\hbar\sum_l \frac{d\alpha_l(t)}{dt}u_l(\vec{r})e^{-i\omega_l t}+i\hbar\sum_l (-i\omega_l)\alpha_l(t)u_l(\vec{r})e^{-i\omega_l t} \qquad (2.2.10)$$
$$=\sum_l \alpha_l(t)H_0 u_l(\vec{r})e^{-i\omega_l t}+\sum_l \alpha_l(t)V(t)u_l(\vec{r})e^{-i\omega_l t}$$

and since $E_l=\hbar\omega_l$ the second and the third term cancel. To simplify this expression even further, we multiply both sides by the factor $u_m^*(\vec{r})$, we integrate over all space and we get that:

$$\int u_m^*(\vec{r})i\hbar\sum_l \frac{d\alpha_l(t)}{dt}u_l(\vec{r})e^{-i\omega_l t}d^3r=\int u_m^*(\vec{r})\sum_l \alpha_l(t)V(t)u_l(\vec{r})e^{-i\omega_l t}d^3r \quad (2.2.11)$$

By using the orthonormality condition:

$$\int u_m^*(\vec{r})u_l(r)d^3r=\delta_{ml} \qquad (2.2.12)$$

we obtain that:

$$i\hbar\frac{d\alpha_m(t)}{dt}=\sum_l \alpha_l(t)V_{ml}e^{-i\omega_m t} \qquad (2.2.13)$$

where $\omega_{lm}=\omega_l-\omega_m$ and

$$\mathrm{V_{ml}}=\int u_m^*(\vec{r})Vu_l(\vec{r})d^3r \qquad (2.2.14)$$

The equation (2.2.13) cannot be solved exactly; therefore we use the perturbation technique where we introduce an expansion parameter λ varying between zero and one. Firstly, we replace V_{ml} by λV_{ml} in (2.2.13) and we expand $\alpha_m(t)$ in a power series as:

$$\alpha_m(t)=\alpha_m^{(0)}(t)+\lambda\alpha_m^{(1)}(t)+\lambda^2\alpha_m^{(2)}(t)+... \qquad (2.2.15)$$

Now, we equate powers of λ on each side of the resulting form of the equation (2.2.13) and we get:

$$\frac{d\alpha_m^{(N)}(t)}{dt} = \frac{1}{i\hbar}\sum_l \alpha_l^{(N-1)}(t) V_{ml} e^{-i\omega_{lm}t} \quad \text{N=1,2,3...} \qquad (2.2.16)$$

where N corresponds to a first order interaction in the field, the second order and etc.

Briefly, multiphoton fluorescence offers several advantages for imaging cells in many biological samples as its excitation requires the quasi-simultaneously absorption of multiple photons, usually two to fulfill the energy requirement. For this process was used ultrafast laser pulse in order to achieve very large peak intensities.

Chapter References

1. O. Svelto, *Principles of Lasers (Fifth Edition)*, Springer Science + Business Media, New York (2010).

2. B.R. Masters and P.T.C. So (Ed.), *Handbook of Biomedical Nonlinear Optical Microscopy*, Oxford Univ. Press, New York (2008).

3. R.W. Boyd, *Nonlinear Optics (Third Edition)*, Academic Press, Burlington, MA (2008).

4. A.F.J. Levi, *Applied Quantum Mechanics (Second Edition)*, Cambridge Univ. Press, New York (2006).

5. Coherent Laser Group*, Multiphoton Excitation Microscopy*, Santa Clara, CA 95054 (2000).

6. M. Oheim, D. J. Michael, M. Geisbauer, D. Madsen, and R. H. Chow, "Principles of two-photon excitation fluorescence microscopy and other nonlinear imaging approaches," *Advanced Drug Delivery Reviews*, vol. 58, no. 7, pp. 788–808, 2006.

7. M. Born and E. Wolf, *Principles of Optics: Electromagnetic Theory of Propagation, Interference and Diffraction of Light*. CUP Archive, 1999..

8. S.Mulligan, and B.MacVicar, "Two-photon fluorescence microscopy: basic principles, advantages and risks," in Modern Research and Educational Topics in Microscopy , A. Méndez-Vilas, and J. Díaz, eds. (FORMATEX, Badajoz, Spain, 2007), pp. 881-889.

Chapter 3. Experimental Apparatus

3.1 Experimental set up

The nonlinear microscope configuration that was used in the examined biological samples, *C.elegans,* is illustrated in figure 3.1.1. The NIR irradiation originated from an amplitude system Yb femtosecond t - pulse laser (1028nm, 50MHz, 1W, 200fs ; t-pulse, Amplitude Systems). Then the laser beam passed through a couple of adjustable neutral density filters in order to control the power at the sample plane and a set of galvanometric mirrors which were placed on a modified upright optical microscope, scanning the biological sample in the X-Y plane. The first mirror moves the laser beam in horizontal place and the second in the vertical plane .The laser beam also was expanded approximately six times with a telescope system which was used to fill the back aperture of the objective lens. Consequently was tightly focused on the sample plane by using high numerical aperture objective lenses (NA$\geq$0.8) to achieve refraction limited focusing. NA is important because it indicates the resolving power of a lens. The size of the finest detail that can be resolved is proportional to 0.6 λ/NA, where λ is the wavelength of the light. A lens with a larger numerical aperture would be able to visualize finer details than a lens with a smaller numerical aperture. Assuming quality (diffraction limited) optics, lenses with larger numerical apertures collect more light and will generally provide a brighter image, but this will provide shallower depth of field. During the experimental process the examined biological samples were placed between two thin (~70nm) round glass slides, separated with a ~100μm thick spacer so any kind of damages were avoided. Both scanning and data acquisition procedures controlled by a Lab View interface. A CCD camera (PixeLINK) was used for observation of the specimens. THG or SHG and TPEF nonlinear signals are simultaneously generated at the selected focal plane and are detected from different channels, one in transmission mode and the other in reflection mode. TPEF signals were recorded via the reflection mode by using a photomultiplier (PMT), which is attached at the position of the microscope and connected to a computer. THG is in the near ultraviolet (UV) part of the spectrum (~343nm) and SHG signal is in visible part of spectrum (~514nm).

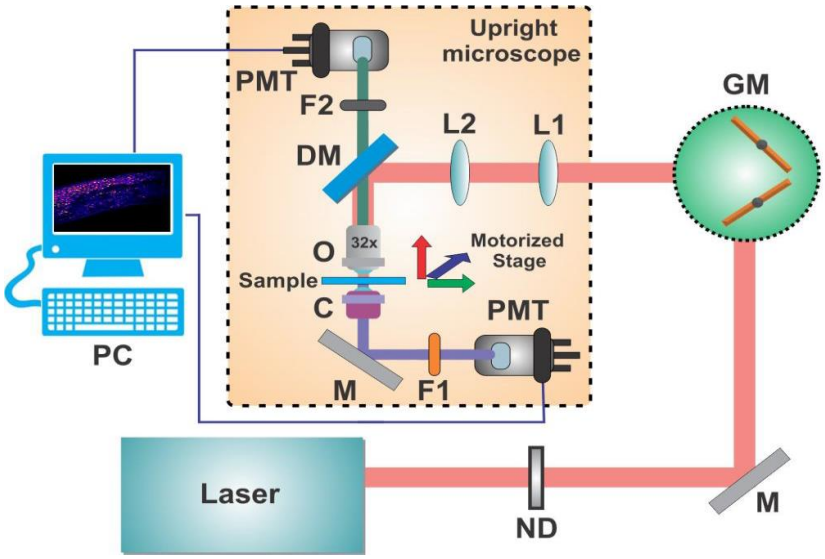

Figure 3.1.1*: Representation of the nonlinear microscope configuration. The detection paths are two: one in the reflection (for the TPEF signals) and the other in the transmission mode (for the SHG and THG signals). ND: Neutral Density filters, M: Mirrors, GM: Galvanometric Mirrors, L1, L2: telescope lenses, DM: Dichroic mirror, O: objective, C: condenser, F1, F2: filters, PMT: photomultiplier tube, PC: computer.*

In case of calibration the photomultiplier tube is connected to a Lock in Amplifier (SR810 Stanford Research Systems). Lock-in amplifiers are used to measure the amplitude and phase of the signals buried in noise. They achieve this by acting as a narrow bandpass filter, which removes much of the unwanted noise while allowing through the signal that is to be measured. Choppers are often used together with lock-in amplifiers. Optical choppers are used to modulate light beams or particle streams. By modulating the optical beams or particle streams, optical choppers allow these signals to be measured accurately in environments with high ambient noise. Therefore, the use of a Lock in Amplifier provides a very good noise rejection, and measurements can be performed in less stringent lighting conditions. However, Lock in Amplifier wastes a lot of time to measure signals that is why we use it only at calibration progress. Furthermore, a short pass filter (SPF 700 nm, CVI) is placed at the PMT input to cut off the reflected laser light.

THG signal is collected in transmission mode by the condenser lens. Condensers are located above the light source and under the sample in an upright microscope,. They act to gather light from the microscope's light source and concentrate it into a cone of light that illuminates the specimen. The condenser lens system should have an N.A. greater than or equal to the largest NA of the objectives. The higher the power, the more important this *condenser lens* becomes. Most of harmonic generation light in case of thin samples propagates with the fundamental laser beam. After passing through a colored glass filter (U 340-Hoya), the THG transmission at

343nm or SHG reflection at 514nm signal reached a second PMT tube (Hamamatsu) and were recorded simultaneously from the same computer. When we combined THG and SHG signal, the first one was collected in transmission mode applying 343nm filter and the second one in reflection mode applying 514nm interference filter. In case of fluorescence signal, it was collected in reflection mode. The focal plane was selected with a motorized translation stage (Standa, 1 κm minimum step). A high resolution THG/SHG or TPEF scan was performed in less than two seconds by the employed setup.
In order to improve the signal to noise ratio, each image results from the simple averaging of several scans. Thus, the total required time to obtain a single image was ranging from 8 to 35 seconds depending on the resolution and the number of the averaging frames. Image J (NIH, http://imagej.nih.gov/ij/) was used for viewing and processing the obtained data. For the generation of maximum Z-projections or the respective three dimensional reconstructions of the examined samples, a series of sequential slice images were acquired at 2 μm intervals (Z-stack).

Femtosecond laser pulses

The main building block for generating femtosecond pulses is lasers. They were used for generating ultrashort pulses in the picosecond and also in femtosecond time domain. In a general way, a pulse can be defined as a transient in a constant background. The shape of this pulse is the shape of this transient. Therefore, the pulse shape can be represented by a bell-shaped pulse function, such as a Gaussian function. As it is known that the Fourier transform of the Gaussian function is also a Gaussian function, the general time and frequency Fourier transforms of a pulse can be written:

$$E(t) = \frac{1}{2\pi} \int_{-\infty}^{+\infty} E(\omega) e^{-i\omega t} d\omega \qquad (3.1.1)$$

and

$$E(\omega) = \int_{-\infty}^{+\infty} E(t) e^{i\omega t} dt \qquad (3.1.2)$$

where $E(\omega)$ and $E(t)$ represent the frequency and the time evolution of the electric field of the pulse, respectively. The relationship between the duration and the spectral bandwidth of the laser pulse can be written as:

$$\Delta v \Delta t \geq K \qquad (3.1.3)$$

where Δv is the frequency bandwidth measured at full-width at half-maximum (FWHM) with $\omega = 2\pi v$ and Δt is the FWHM in time of the pulse and K is a constant number which depends only on the pulse shape and determines the time-bandwidth product.

Thus, to generate a laser pulse within femtosecond time domain one needs to use a broad spectral bandwidth. If the quality is reached in (3.1.3) has to do with a Fourier-transform-limited pulse or simply a *transform limited pulse*. This can also calculate the minimum time duration of a pulse giving a spectrum with $\Delta\lambda\ (nm)$ at FWHM, central wavelength $\lambda_0\ (nm)$ and the speed of light $(m/s)\ c$:

$$\Delta t \geq K \frac{\lambda_0^2}{\Delta\lambda \cdot c} \qquad (3.1.4)$$

Femtosecond laser pulses can be generated directly from a wide variety of lasers with wavelengths ranging from the ultraviolet to the infrared. The characterization of ultrashort pulses with respect to amplitude and phase is therefore based on optical correlation techniques that make use of the short pulse itself. Methods operating in the time-frequency domain are especially useful.

Gaussian beams

Gaussian beam is an incident radiation that is focused as a laser beam in a nonlinear medium in order to increase the intensity and hence the efficiency of the nonlinear optical processes. It can be described by a nonlinear optical wave equation:

$$\vec{\nabla}^2 \vec{E} - \frac{n^2}{c^2} \frac{\partial^2 \vec{E}}{\partial t^2} = \mu_0 \frac{\partial^2 \vec{P}^{NL}}{\partial t^2} \qquad (3.1.5)$$

In this case the electric and polarization field $\vec{E}_n$ and $\vec{P}_n$ respectively are expressed as:

$$\vec{E}_N(\vec{r},t) = \vec{A}_N(r) e^{i(k_N z - \omega_N t)} + c.c. \qquad (3.1.6)$$

$$\vec{P}^{NL}(\vec{r},t) = \vec{p}_N(r) e^{i(k'_N - \omega_N t)} + c.c. \qquad (3.1.7)$$

where we allow the complex amplitudes A_n and p_n to be spatially varying quantities, therefore $\vec{E}_N$ and $\vec{P}^{NL}$ to represent non-plane waves. Additionally the possibility of a wave vector is allowed to mismatch, by allowing the wave vector of $\vec{P}^{NL}$ to be different than that of $\vec{E}_N$. Furthermore, the z direction had been specified to be the dominant direction of propagation of the wave $\vec{E}_N$, so that it could be easily expressed by the Laplace operator as:

$$\vec{\nabla}^2 = \frac{\partial^2}{\partial z^2} + \vec{\nabla}_T^2 \qquad (3.1.8)$$

The second term represents the transverse Laplacian and is given by:

$$\vec{\nabla}_T^2 = \frac{\partial^2}{\partial x^2} + \frac{\partial^2}{\partial y^2} \qquad (3.1.9)$$

Thus, by substituting equations (3.1.6) and (3.1.7) into (3.1.5), the Laplacian could be replaced and make a varying amplitude approximation. The final equation becomes:

$$2ik_N \frac{\partial \vec{A}_N(r)}{\partial z} + \vec{\nabla}_T^2 \vec{A}_N(r) = -\frac{\omega_N^2}{\varepsilon_0 c^2} \vec{p}_N(r) e^{i\Delta kz} \qquad (3.1.10)$$

where $\Delta k = k_N' - k_N$ (3.1.11) is the wave vector mismatch.

The transverse intensity distribution that is everywhere Gaussian can be represented in that scalar approximation as an electric component:

$$A(r,z) = A_0 \frac{w_0}{w(z)} e^{-r^2/w(z)^2} e^{ikr^2/2R(z)} e^{i\phi(z)} \qquad (3.1.12)$$

Where

$$w(z) = w_0 \left[1 + (\lambda z / \pi w_0^{\,2})^2\right]^{1/2} \qquad (3.1.13)$$

represents the $1/e$ radius of the field distribution, where

$$R(z) = z\left[1 + (\pi w_0^2 / \lambda z)^2\right] \qquad (3.1.14)$$

is the wavefront radius of curvature after propagating distance z and:

$$\varphi(z) = -\arctan\left(\frac{\lambda z}{\pi w_0^2}\right) \qquad (3.1.15)$$

is the phase that is associated with the spatial and the temporal change of the curvature of the wavefront known as Gouy shift.

Extensively, r represents the radial distance from the center axis of the beam and z is the distance propagated from the plane, λ represents the wavelength of light and w_0 represents the radius of the $1/e^2$ irradiance contour at the plane wave haw propagated a distance z. R(z) is infinite at z=0, passes through a minimum at some infinite z, and rises again toward infinity as z is further increased, asymptotically and approaching the value of z itself. The plane z=0 marks the location of a Gaussian waist or a place, where the wavefront is flat, and w0 is called the beam waist radius.

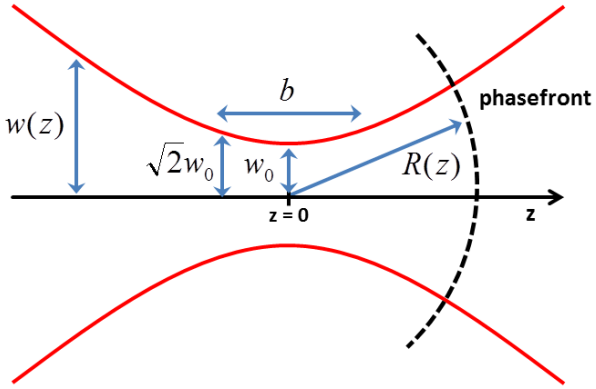

Figure 3.1.2: *Gaussian beam width w(z) as a function of the axial distance z, w_0 is the beam waist radius, b the confocal parameter and R(z) the radius of curvature of the optical phasefront.*

In a convenient way, we are able to represent the Gaussian beam in a compact form:

$$A(r,z) = \frac{A_0}{1+i\zeta} e^{-r^2/w_0^2(1+i\zeta)} \qquad (3.1.16)$$

$\zeta = \frac{2z}{b}$ b (3.1.17) is the longitudinal coordinate defined in terms of the confocal parameter $b = \frac{2\pi w_0^2}{\lambda}$ (3.1.18) from where the longitudinal extend can be measured.

The total power P carried by a Gaussian laser beam can be calculated by integrating over the transverse intensity distribution of the beam and is given by:

$$P = \int I 2\pi r \, dr \qquad (3.1.19)$$

where the intensity is given by $I = 2n\varepsilon_0 c\pi w_0^2 |A|^2$. Thus, by substituting it into (3.1.19) we get:

$$P = n\varepsilon_0 c\pi w_0^2 |A|^2 \qquad (3.1.20)$$

A Gaussian fundamental beam constitutes the main resource for harmonic generation. In case of N-th harmonic generation, the nonlinear polarization is expressed by equation:

$$p_N(r) = \varepsilon_0 \chi^{(N)} (A_1(r,z))^N \qquad (3.1.21)$$

The complex amplitude $A_1(r,z)$ is described as:

$$A_1(r,z) = \frac{A_0^{(1)}}{1+i\zeta} e^{-r^2/w_0^2(1+i\zeta)} \qquad (3.1.22)$$

The solution of optical wave equation in case of N-th harmonic is the trial one:

$$A_N(r,z) = \frac{A_0^{(N)}(z)}{1+i\zeta} e^{-Nr^2/w_0^2(1+i\zeta)} \qquad (3.1.23)$$

Here, we have to notice that the trial solution (3.1.23) deals with a beam with the same confocal parameter b as the fundamental one. This means that the harmonic wave of N-th order is coherently generated over a region whose longitudinal extend is equal to the fundamental wave.

The substitution of (3.1.22) into (3.1.10) gives:

$$2ik_N \frac{\partial A_N(r,z)}{\partial z} + \nabla_T^2 A_N(r,z) = -\frac{\omega_N^2}{c^2} \chi^{(N)} (A_1(r,z))^N e^{i\Delta kz} \qquad (3.1.24)$$

now, the vector mismatch is given by:

$$\Delta k = Nk_1 - k_N \tag{3.1.25}$$

By substituting equation (3.1.23) into (3.1.24) we find that the equation is satisfied if:

$$\frac{\partial A_0^{(N)}}{\partial z} = \frac{iN\omega}{2n_N c}\chi^{(N)}(A_0^{(1)})^N \frac{e^{i\Delta kz}}{(1+i\zeta)^{N-1}} \tag{3.1.26}$$

From the above equation we obtain the relationship:

$$A_0^{(N)} = \frac{iN\omega}{2n_N c}\chi^{(N)}(A_0^{(1)})^N J_N(\Delta k, z_0, z) \tag{3.1.27}$$

where,

$$J_N(\Delta k, z_0, z) = \int_{z_0}^{z} \frac{e^{i\Delta kz'}}{(1+2iz'/b)^{N-1}} dz' \tag{3.1.28}$$

Here, z_0 gives us the value of z at the entrance to the nonlinear medium.
The integral (3.1.28) in case of the plane wave limit, where $b >> |z_0|, |z|$ reduces to:

$$J_N(\Delta k, z_0, z) = \int_{z_0}^{z} e^{i\Delta kz'} dz' = \frac{e^{i\Delta kz} - e^{-i\Delta kz_0}}{i\Delta k} \tag{3.1.29}$$

which implies that:

$$\left|J_N(\Delta k, z_0, z)\right|^2 = L^2 \sin c^2\left(\frac{\Delta kL}{2}\right) \tag{3.1.30}$$

$L = z - z_0$ is the length of the interaction region.
On the other hand, when the fundamental wave is tightly focused within the volume of the medium so that $b << |z_0|, |z|$, we can replace the integration limit of (3.1.28) by plus and minus infinity:

$$J_N(\Delta k, z_0, z) = \int_{-\infty}^{\infty} \frac{e^{i\Delta k z'}}{(1+2iz'/b)^{N-1}} dz' \qquad (3.1.31)$$

After integration we get:

$$J_N(\Delta k, z_0, z) = \begin{cases} 0 & ,\Delta k \le 0. \\ \frac{b}{2} \cdot \frac{2\pi}{(N-2)!} \left(\frac{b\Delta k}{2}\right)^{N-2} e^{-b\Delta k/2}, & \Delta k > 0. \end{cases} \qquad (3.1.32)$$

At this point, the equation (3.1.32) maintains a lively interest. In case of THG (N=3) the efficiency in the tight-focusing limit vanishes where the phase matching condition is met (Δk=0) and is maximized through the use of a positive mismatch value (Δk>0). This result can be understood in terms of the Gouy phase shift by π radians, which is experienced by any beam that passes through its focus.

For example, when a focused Gaussian laser beam of angular frequency ω interacts within a nonlinear medium of third order susceptibility $\chi^{(3)}$ where the perfect phase matching condition is fulfilled (Δk=0), the electric fields before and after the beam waist position will be described by opposite functions , as a result of the π radians phase shift and the same is accepted for their respective third order nonlinear polarizations which depend on the cube of the incident field. In order to obtain noticeable THG signal, a non-zero Δk is required which implies the inequality $n_\omega \neq n_{3\omega}$. This exists in normal dispersive materials since always $n_{3\omega} > n_\omega$.

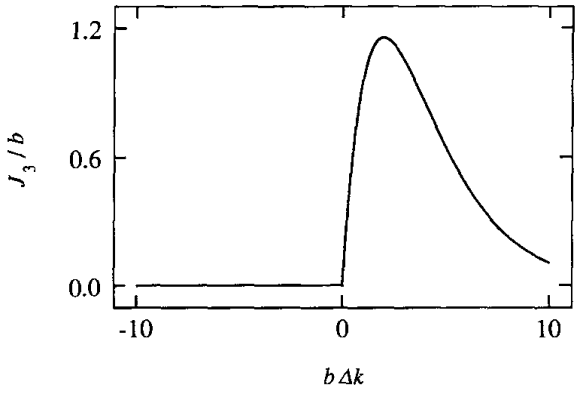

Figure 3.1.3*: Dependence of the phase-matching factor J3 for third-harmonic generation on the normalized confocal parameter b Δk, in the tight-focusing limit.*

Now, getting N=2 in equation (3.1.32), in case of tight focusing, the efficiency of SHG is maximized when is maximized when an infinitely small positive phase mismatch Δk is introduced (practically zero). Hence, the SHG procedure excited by tightly focused Gaussian

beams requires that the phase matching condition (3.1.25) is fulfilled, similarly to the case for plane wave excitation. This can be practically achieved by making use of the birefringence presented by several materials having dependence of the refractive index on the polarization of the incident light. As far as SHG microscopy is concerned, the biological structures that present the necessary conditions (non-centrosymmetric molecules and birefringence) for the effective generation of second harmonic signal are collagen, myosin fibrils, tubulin etc.

As we all know, photons have energy and momentum that are conserved when optical harmonics generation procedure is taking place and they are also characterized by wave vector $\vec{k}$ (1.1.3). In third harmonic generation procedure (THG), the energy conservation is satisfied since the energy of the resulting photon 3ω is equal to the energy sum of the three initial photons having angular frequency ω. As far as photon momentum conservation is concerned, the vector sum of the momenta of the three initial photons (characterized by wave vectors $\vec{k}_{\omega}^{(1)}$, $\vec{k}_{\omega}^{(2)}$ and $\vec{k}_{\omega}^{(3)}$ respectively) must be equal to the momentum vector of the THG photon $\vec{k}_{3\omega}$:

$$\hbar\vec{k}_{3\omega} = \hbar(\vec{k}_{\omega}^{(1)} + \vec{k}_{\omega}^{(2)} + \vec{k}_{\omega}^{(3)}) \qquad (3.1.33)$$

Concentrating in case of THG, there is a collection of angularly spread wave vectors within an angular range that depends on the numerical aperture of the focusing lens, which constitute the focused Gaussian laser beam. Therefore, equation (3.1.33) could be valid for Δk=0 and due to the totally destructive interference taking place during perfect phase matching conditions, no THG signal can be obtained. Momentum conservation cannot be satisfied by any way for Δk<0 and as a result THG is not possible for normal dispersive materials where $n_{3\omega}>n_{\omega}$. Efficient THG signal can occur since three of the angularly spread wave vectors can combine ,so that the equation (3.1.33) to be successfully fulfilled. This is valid for Δk>0 and thus $n_{3\omega}<n_{\omega}$. In practice, the required inequality $n_{3\omega}<n_{\omega}$ can be met if the beam is focused on an interface of two materials having different refractive index values for fundamental and THG wavelengths respectively.

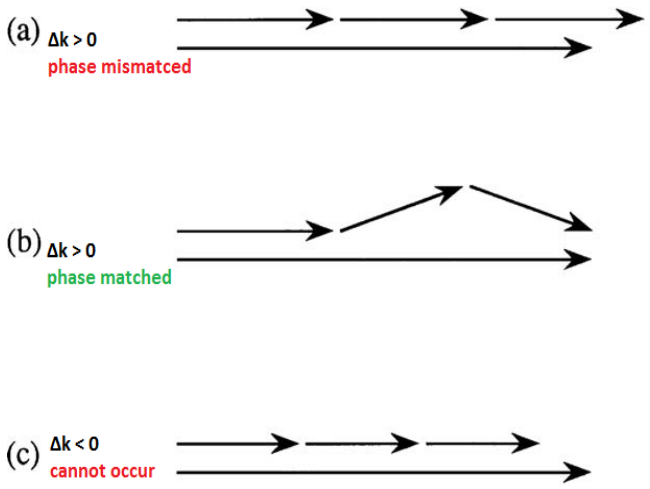

Figure 3.1.4: *a) THG process is phase-mismatched and no efficiency is taken place. b)For perfect phase matching, the momentum conservation of the photons can be met as we see in the wave vector diagram ,where the fundamental beam can be added effectively and THG signal is generated. If $n_{3\omega}<n_{\omega}$, efficient THG can occur since the angularly spread wave vectors of fundamental beam can be added effectively so that the total momentum before and after the nonlinear interaction to be conserved. c) Momentum conservation condition cannot be met (for normal dispersive materials ($n_{3\omega}>n_{\omega}$)), therefore THG is not possible.*

Either a third order susceptibility or a refractive index interface, which will ensure that the resulting harmonic waves will not interfere totally destructively during their propagation along the medium, results an effective generation of third harmonic light signal by a focused Gaussian laser beam. The conditions that we mentioned before could be simultaneously met and make THG microscopy an ideal tool for the in-vivo examination of the structure and morphology of various optically inhomogeneous biological specimens.

Chapter References

1. F. Trager (Ed.), *Springer Handbook of Lasers and Optics*, Springer Science + Business Media, New York (2007).

2. D.B. Murphy, *Fundamentals of light microscopy and electronic imaging*, Wiley-Liss, New York (2001).

3. R.W. Boyd, *Nonlinear Optics (Third Edition)*, Academic Press, Burlington, MA (2008).

Chapter 4. Biological Sample

4.1 Caenorhabditis elegans (*C. elegans*)

The simple body plan and transparent nature of both the egg and the cuticle have facilitated the exceptionally detailed developmental and anatomical characterization of this animal. The complete sequence of cell divisions and the normal pattern of programmed cell death events that occur as the fertilized egg develops into the 959-celled adult are known. *C. elegans* is the first metazoan for which the genome was sequenced to completion.

Figure 4.1.1: Configuration of the transparent biological sample *C. elegans.*

An important advantage of this experimental model organism is that construction of transgenic animals is rapid. DNA injected into the hermaphrodite gonad concatamerizes and is packaged into embryos in the form of an extra chromosomal array. Hundreds of progeny can be obtained within a few days of the injection. The anatomical characterization and understanding of neuronal connectivity in *C. elegans* is unparalleled in the metazoan world. Serial section electron microscopy has identified the pattern of synaptic connections made by each of the 302 neurons of the animal (including 5000 chemical synapses, 600 gap junctions, and 2000 neuromuscular junctions), so that the full "wiring diagram" of the animal is known. Overall, the broad range of genetic and molecular techniques applicable in *C. elegans* allows a unique line of investigation into fundamental problems in biology.

Chapter 5. Colocalization THG signals with lipid staining particles in *C. Elegans*.

5.1 Introduction

Most biological tissues exhibit optical properties that are dependent of light penetration, such as refraction index, scattering factor, anisotropic factor and the laser absorption in tissues. In principle, four phenomena provide the undistributed propagation of light in tissues: reflection, scattering, absorption and fluorescence. Therefore, when biological tissue is irradiated by laser light, is responsible for an individual function. Namely, a small fraction of light is reflected, but most of it penetrates into tissue, where it is either absorbed or scattered by molecules [1].

Molecules and biomolecules such as triacylglycerols (TAGs) and cholesterol ester (CE) that can be found in neutral fat, form lipid droplets in mammalian cells. These cytoplasmic organelles can be detected in all cells and their diameter varies from hundreds of nanometers to several micrometers [2]. Macrophage lipid storage displays an important role in health and concatenates with the process of atherosclerosis [3] and other epidemics such as obesity's molecular mechanisms [4] and fatty liver disease [5]. At this point it is important to detect lipids and be able to distinguish different lipid species at the cellular level. Therefore, nonlinear optical microscopy techniques based on third harmonic generation (THG) and coherent anti-Stokes Raman scattering are very useful for label-free imaging of lipid droplets [6,7] in cells and tissues, while it requires a careful use of laser sources [8]. CARS microscopy detects molecules based on chemical selectivity such as a high density of aliphatic compounds in lipids [9, 10]. A recently developed nonlinear microscopy technique that has been designed to overcome the limitations of CARS, is the stimulated Raman scattering (SRS). This technique provides a good quality of cell or tissue images but it might be costly. Due to the fact that several media have optical heterogeneities for example, water and lipid interfaces in biological samples, THG signals are different and result in a high contrast signal arising from lipid droplets, requiring a single pulsed laser source [11,7]. In addition, another study has shown that both the object size and the beam focusing play an important role to the signal that it arises from a small object.

Therefore, there is an influence of the focusing conditions on the signal generated from different structures within the sample. As a result, when a beam is focused at the interface between two semi-infinite media with normal dispersion, the signal gets the scale as the third power of the intensity at the interface. In case of mouse embryos, the signal of a tightly focused beam arises from the external membrane, whereas for a more weakly focused beam the signal arises from internal μm sized organelles so there is an enhancement of certain structures in THG imaging [13]. Additionally, THG microscopy with polarized light also provides the visualization of lipid droplets because of its symmetry properties. The identification and discrimination between lipid droplets of different lipid depositions at subcellular resolution can be achieved by linearly and circularly polarized input beam [2]. Another advantage of THG microscopy is that it provides images from unstained cells and tissues giving complementary information to fluorescence by changing the third-order nonlinear susceptibilities, refractive index and dispersion. Specifically, interfaces and heterogeneities between two media originated from different linear and nonlinear properties can be also detected. These changes in third-order nonlinear susceptibility values are quantified for many solvents (water, ethanol, glycerol), physiological aqueous (ions, glucose, amino acids) and lipid (triglycerides, cholesterol) [12]. The advantages of non-linear techniques such as, second harmonic generation (SHG), third harmonic generation (THG), coherent anti-Stokes Raman scattering (CARS), and stimulated Raman scattering (SRS) including two-photon excitation fluorescence (TPEF), are comparable to other microscopic techniques that provide the capability of intrinsic three-dimensionality (3D), increased axial resolution, the ability to section deep within tissues and the reduction of out of focus photobleaching and phototoxicity in the specimens.

In the current work we tried to clarify the use THG microscopy to image lipids *in vivo* in order to necessitate it as a powerful, label-free alternative technique evolved in a microscope set up which simultaneously images fluorescence and higher harmonic generation signals eliding staining with dyes and other fluorescent markers. Imaging specimens has been achieved by a single laser beam, but specific chemical or molecular information could not be provided. Lipid droplets are structures that seem to have great importance in THG microscopy as they are basic structures for detection of high THG signals and its visualization has been used as a tool to

identify genes that control fat storage [26, 27]. THG signals are effectively generated by formations that present optical discontinuities regarding the linear refractive index and/or the third order susceptibility values $\chi^{(3)}$ as to the surrounding watery environment in the *C. elegans* body. By performing this kind of measurements, information related to the anatomy and the morphology of the worm was extracted. However, optical discontinuities due to lipid depositions provide significantly more intense THG signals which can be up to an order of magnitude higher when compared to other structures such as membranes and mitochondria under the same illumination conditions. Therefore, lipid droplets can be effectively isolated from the surrounding recorded structures by thresholding the stack of the obtained images during the processing of the data. Previous studies have shown that THG imaging has been used to image lipid depositions focusing on optical discontinuities and as a result generating significantly intense THG signals [14]. Additionally, it has been used to image lipid depositions in plant seeds, *Drosophila* embryos, cell lines and rat hepatocytes [15, 16, 12, 14]. Consequently, THG imaging modality forms a non-destructive imaging technique and a useful diagnostic tool to provide in details structural and morphological information for various specimens. It has been achieved monitoring the developmental processes of embryogenesis of many biological settings and quantitative cell tracking studies at early stage embryos via the detection of higher harmonic signals [17, 18, 19, 20].

In the current study, we brought the THG signal into focus to distinguish whether it comes from lipids or another intrinsic autofluorescent organelles and regions of nematode *C. Elegans*. In previous chapter we mentioned the reasons why we used nematode *C. Elegans* for our measurements. Concisely, it is transparent and permits microscopic visualization of specific cells and sub-cellular structures. As well as the anatomical information is available for the entire animal and the nervous system wiring diagram is fully known, we are able to study the biological processes at the whole animal level of *C. Elegans* .

Consequently, we are able to show the colocalization of fluorescent and THG signals by using specified lipid staining dyes Bodipy 500/510, Nile Red and Oil Red-O. To this effect, we excluded the proposition that lipofuscin was contributing to the THG signal from the animal. So, we propose THG to be a powerful, easily acquired technique to detect lipids in all organisms,

investigate cellular and molecular mechanisms controlling fat storage and metabolism in the near future.

5.2 Materials and Methods

5.2.1 *C. Elegans* strains and maintenance

Standard procedures for *C. Elegans* maintenance were followed. All of the samples were provided by Prof. Nektarios Tavernarakis Laboratory at IMBB-FORTH. Briefly, worms were kept at 20 ^{o}C and maintained on standard NGM plates seeded with E. coli OP50 bacteria unless otherwise noted. The strains used include Bristol N2 isolate, wild-type. To investigate wheteher THG signal arises from lysosomes, we used the transgenic animal, RT258: *unc-119(ed3)III , pwls*50[$p_{lmp\text{-}1}$LMP-1::GFP+Cbr-unc-119(+)].

5.2.2 Lipid staining

For the colocalization experiments *C.elegans* stained with three different dyes and N2 Bristol isolate strains were used. The staining process included aliquots of 5 mM Bodipy 500/510 (Sigma, MO) diluted in 100% DMSO were stored in -20 ^{o}C. NGM plates were seeded with OP50 E.coli bacteria and allowed to dry overnight at room temperature. The next day, the bacteria were killed using 48 W UV 254 nm irradiation lamps for 10 min (Bio-Link BLX-E365, Vilber Lourmat, France). Subsequently, 1 μM Bodipy, calculated to the volume of the plate, was squirted onto the surface of the plate and allowed to dry at room temperature. L4 N2 worms were incubated on these plates and transferred to fresh plates every other day until they reached day 4 of adulthood. For epifluorescence and THG imaging, worms were anesthetized with 10 mM sodium azide and mounted on glass slides.

Aliquots of 50 mM Nile Red (Sigma, MO) diluted in 100% DMSO were also stored in -20 ^{o}C. As described above, L4 N2 worms were incubated on plates seeded with UV-killed OP50 bacteria and transferred to fresh plates every other day until they reached day 4 of adulthood. Prior to viewing, worms were fixed for 5 min in 3 mL cold (-20oC) methanol. Subsequently, 2 mL of

PBTw (PBS with 0.1% Tween-20) were added and tubes were centrifuged for 2 min at 3000 rpm to remove the supernatant. Finally, worms were washed twice in PBTw. Following fixation, worms were stained in 10 μM Nile Red for 20 min.

Oil Red-O solution was prepared by adding 0.5 g in 100 mL isopropanol and allowing it to slowly dissolve on the bench for several days. A new solution consisting of 40% stock solution and 60% distilled water was allowed to sit for 10 min and subsequently filtered with a 0.4 μm filter (O"Rourke et al., 2009 CellMetabol). Similar to Nile Red procedures, L4 N2 worms were grown on plates with UV-killed OP50 bacteria and fixed with methanol. For staining, we put worms in a 1:10 (worms in solution: Oil Red-O filtered solution) mixture for 20 min.

5.3 Colocalization

5.3.1 Lipofuscin and THG signals colocalization measurements.

Firstly, we focused on the intestine of *C. Elegans* worms. This region plays an important role in the detection of lipid deposition as there, is gathered the main percentage of lipid droplets. Thus, an issue has been emerged, whether the signal came from lipids or lipofuscin. We performed a colocalization assay where THG and TPEF are simultaneously coupling to image targeting non fluorescent neutral lipid droplets and autofluorescent deposits lipofuscin respectively in order to distinguish the origin of two different signals. Concerning the lipofuscin, is composed of oxidized and cross-linked macromolecules, and advanced glycosylation end products. It is easily detected due to its autofluorescence and is easily found in the intestinal cells of the aging worm. The excitation of lipofuscin was achieved in our set-up via the absorption of two photons at 1028 nm. Each image consists of twenty-five optical sections taken at 2 μm steps from day 4 adult wild type worms. To determine whether the THG signal colocalizes with lipofuscin, THG and TPEF images were generated and recorded simultaneously as is illustrated in Figure 5.3.1. As verified by the merged image below, THG signal fails to localize with lipofuscin and the resultant deduction is that lipofuscin is not the sub-cellular structure which originates the strong THG signal.

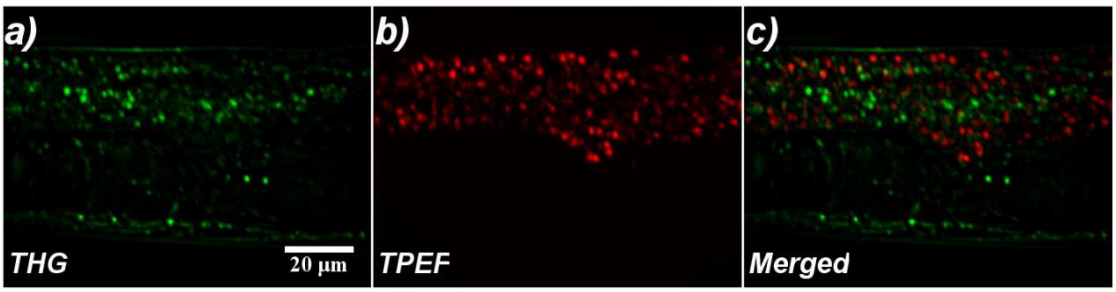

Figure 5.3.1: a) Mid body region of wild type *C.elegans* which is visualized by THG, b) the same sample and region of the animal visualized by TPEF showing lipofuscin and c) merged image denoting the absence of colocalization between lipofuscin (red) and THG signal (green).

5.3.2 THG signals localize with lipid staining.

Lipids in Adipose Fat Tissue

To ensure that lipids originate the THG signal we used lipid-staining dyes to stain the worms. As it is shown in the figure 5.3.2, Bodipy 500/510 dye was the food for the last larval stage of the worm until the 4 day of its adulthood, Nile Red or Oil Red-O was the staining dye for fixed worms exactly the day of imaging. In figures 5.3.2a, 5.3.2d and 5.3.2g we demonstrate the visualized lipids droplets with THG (case 1). In figures 5.3.2b, 5.3.2e and 5.3.2h, are depicted the labeled structures by Bodipy, Nile Red and Oil Red-O respectively which have been visualized by TPEF (case 2) and then the merged images (Figure 5.3.2c, 5.3.2f and 5.3.2i) confirm the fact that the visualized structures in case 1 are associated with lipid droplets. As a result, we proved that the lipid bodies are the main sub-cellular structures that give strong THG signals in the region of intestine in worm and finally THG depicts lipid stores in *C. Elegans* worms.

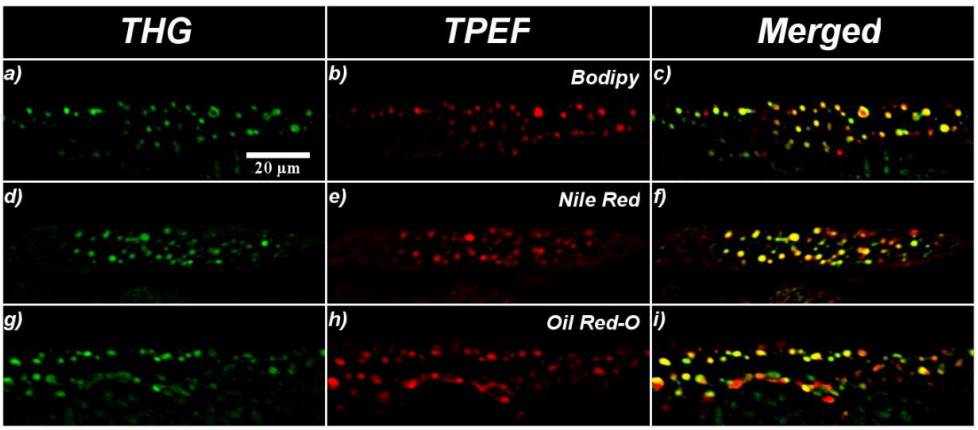

Figure 5.3.2: In a), d) and c) are illustrated lipid droplets visualized by THG in the intestine of *C. Elegans (green).* b), e) and h) are in context images obtained by TPEF stained by *Bodipy 500/510* , *Nile Red* and *Oil Red-O* respectively *(red)*. c), f) and i) are the colocalization images of THG with TPEF *(yellow)* stained with the *Bodipy 500/510* , *Nile Red* and *Oil Red-O* dyes. Lipids are the structures visualized by THG.

Lipids in Non-adipose Fat Tissue

This combination of THG and TPEF fluorescence give us a chance to investigate also the origin of THG signals from lipid droplets stored in non-adipose tissue. We imaged worms fixed and stained with Nile Red, a fluorescent dye was used for fat content visualization in nematodes [28]. In the figures below, we found that THG and TPEF signals colocalized in the pharyngeal muscles of fixed animals, indicating that a strong THG signal emanates from ectopically distributed lipid droplets (Fig.5.3.3). There are no changes in the intensity or the localization of THG signals collected from muscular areas were monitored in animals stained with Nile Red.

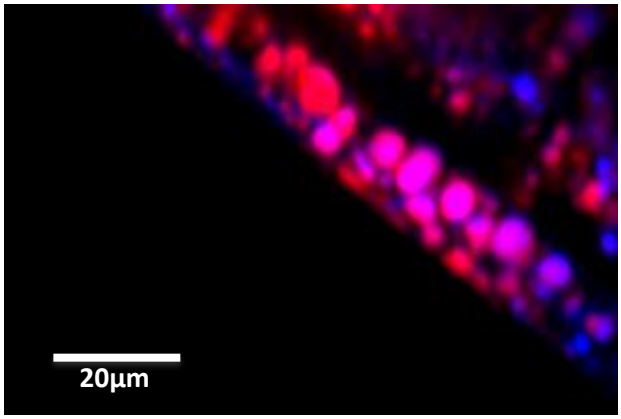

Figure 5.3.3: Fixed 15 days old wild type *C.elegans* where THG (*blue*) and TPEF (*Nile Red, red*) are colocalized (*purple*) in the area of pharyngeal muscles where ectopic lipid droplets are depicted.

As it is shown there is a great overlap between THG signal and TPEF even in muscular areas of *C.elegans* where there is a significant accumulation of ectopic fat. This fact ensures that THG signal originates from lipid droplets not only in regions of the animal that are typically fat storage, but also in non-adipose regions respectively. Namely, in Figure 5.3.4 is depicted the lipids of head muscles of the animal and the region of pharynx denoting that there is also a great colocalization between THG and TPEF signal. As a result, we confirmed the existence of ectopic fat in pharyngeal and body wall muscles of the head region of *C.elegans.*

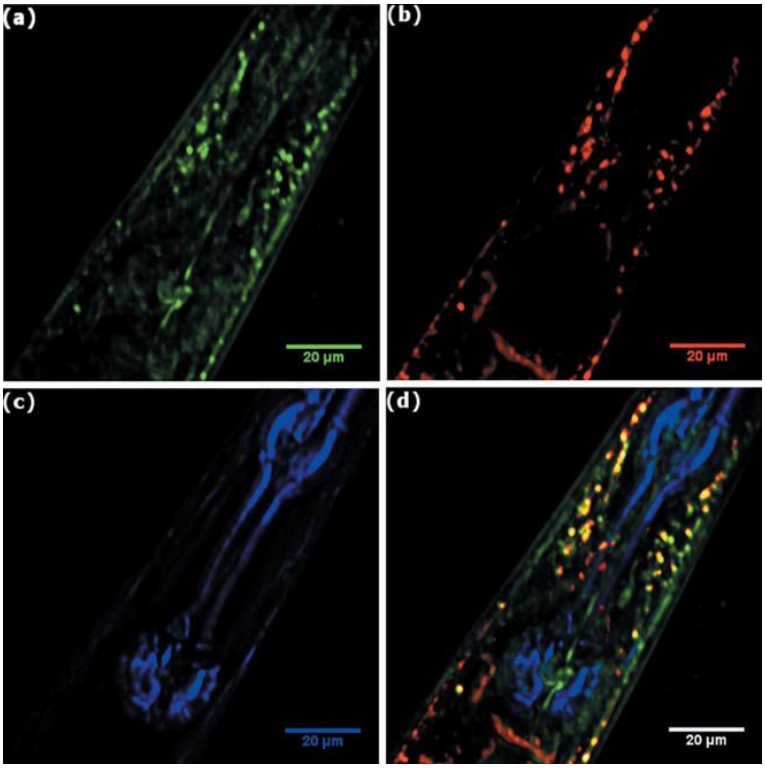

Figure 5.3.4: The head region of 1 day old stained *C.elegans* where is illustrated in a) THG signal *(green)* originated from lipids, b) TPEF *(red)* coming from lipids that stained with *Nile Red* and c) SHG signal *(purple)* that arises from the body wall and pharyngeal muscles. d) is the merged image of all three colors.

Lysosome-related organelles

Except from lipofuscin there are other organelles in nematode *C.elegans* that may extract THG signal. These lysosome-related structures [29] have to be distinguished from the lipid droplets in order to validate the specificity of THG signal. To achieve that, we imaged transgenic animals expressing the lysosomal protein LMP-1 fused with GFP nearby the intestine region (Fig. 5.3.5).

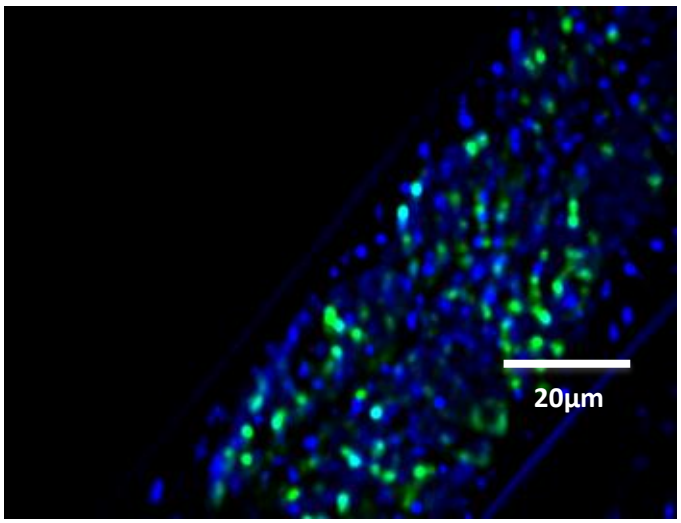

Figure 5.3.5: Expression of the lysosomal protein LMP-1 in transgenic animal fused with GFP, THG signal (*blue*), lysosome-related structures fused with GFP (*green visualized via TPEF measurements*) and no significant colocalization of LMP-1 protein with GFP (*white*).

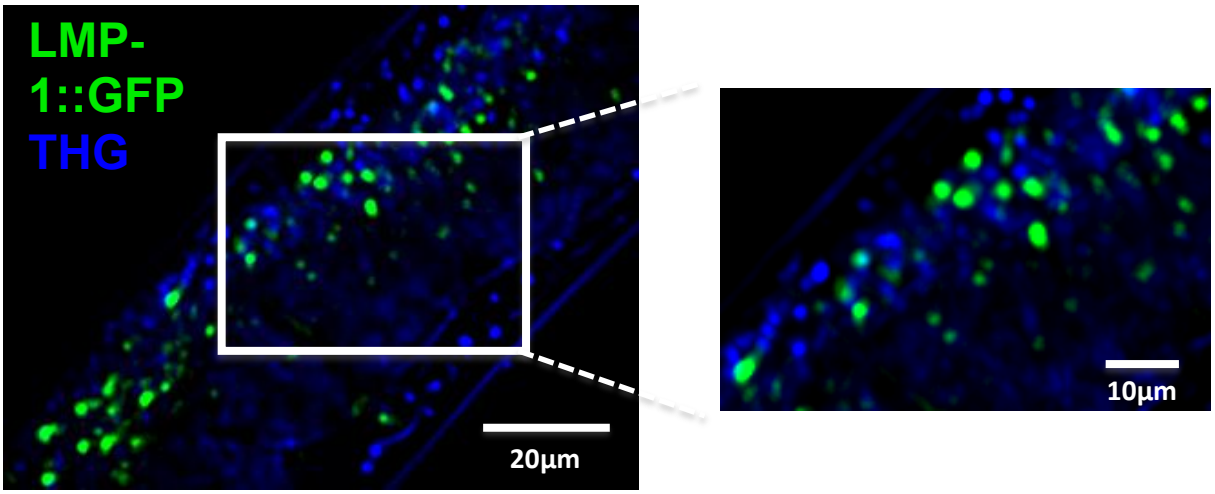

Figure 5.3.6: The colocalization between THG and lysosome-related signals failed.

Figure 5.3.5 and 5.3.6 reveal that THG signal is distinguished from lysosome-related organelles signal.

This result is a confirmation that THG signals in nematode *C.elegans* come from lipid droplets instead of other organelles. Furthermore, we are able to study new applications and combinations in THG or SHG signals in order to investigate lipid accumulation in whole animal either in adipose (fat accumulation in intestine region) or in non-adipose tissue (ectopic fat accumulation in pharyngeal muscles or tail). In the next chapter we are going to show how lipid accumulation correlates with aging using this promising technique also in mutants. The study is focused in adipose tissue of the nematode *C.elegans* where we achieved the visualization of lipid depositions via THG *in vivo*. Moreover, by quantifying THG signal we will show that fat content increases during adulthood.

Chapter References

1. Mechanisms of laser – tissue interaction, I. Optical properties of Tissue, Mohammad Ali Ansari, Ezeddin Mohajerani.
2. Polarized THG Microscopy Identifies Compositionally Different Lipid Droplets in Mammalian Cells, Godofredo Bautista…
3. Moore, K. J. and I. Tabas., 2011. Macrophages in the pathogenesis of atherosclerosis. *Cell*. 145:341-355.
4. Xu, H., G. T. Barnes, …, H. Chen., 2003. Chronic inflammation in fat plays a crucial role in the development of obesity-related insulin resistance*. J. Clin. Invest.* 112:1821-1830.
5. Leroux, A., G. Ferrere, …, A. M. Cassard-Doulcier. 2012. Toxic lipids stored by Kuppfer cells correlates with their pro-inflammatory phenotype at an early stage of steatohepatitis. *J. Hepatol.* 57:141-149.
6. Evans, C. L., and Xie, X. S., 2008. Coherent anti-stokes Raman scattering microscopy: chemical imaging for biology and medicine. *Annu. Rev. Anal. Chem.* (*Palo Alto Calif*). 1:883-909.
7. Débarre, D., Supatto, W., …, Beaurepaire , E., 2006. Imaging lipid bodies in cells and tissues using third-harmonic generation microscopy. *Nat. Methods.* 3:47-53.
8. Rinia, H. A., K. N. Burger, …, M. Müller., 2008. Quantitative label-free imaging of lipid compostiton and packing of individual cellular lipid droplets using multiplex CARS microscopy. *Biophys. J. 102*:1988-1995.
9. Cheng, J., X. (2007) Coherent anti-Stokes Raman scattering microscopy. *Applies Spectroscopy* 61:197-208.
10. Folick, A. , Min, W. , Wang, M., C., 2011. Label-free imaging of lipid dynamics using Coherent Anti-stokes Raman Scattering (CARS) and Stimulated Raman Scattering (SRS) microscopy. *Current Opinion in genetics and & development*. 21: 588-590.
11. Müller, M., J. squire, …, G. J. Brakenhoff., 1998. 3D microscopy of transparent objects using third- harmonic generation. *J. Microsc.* 191:266-274.
12. Débarre, D. , Beaurepaire E., 2007. Quantitative characterization of biological liquids for third- harmonic generation microscopy. *Biophys. J.* 92:603-612.

13. Débarre, D. , Supatto, W., Beaurepaire E., 2005. Structure sensitivity in third-harmonic generation microscopy. *Opt. Lett.* 30: 2134-2136.
14. Débarre, D. , Supatto, W., Pena AM , Fabre, A. , Tordjmann, T., et al., 2006. Imaging lipid bodies in cells and tissues using third-harmonic generation microscopy. *Nat. Meth.* 3:47-53.
15. Chen, H., Wang, H., Slipchenko, M.N., Jung, Y., Shi, Y., Zhu, J., Buhman, K.K., and Cheng, J. X., 2009. A multimodal platform for nonlinear optical microscopy and microspectroscopy, *Optic. Express*. 17: 1282-1290.
16. Segawa, H., Okuno, M., Kano, H., Leproux, P., Couderc, V. and Hamaguchi, H. O., 2012. Label-free tetra-modal molecular imaging of living cells with CARS, SHG, THG and TSFG (coherent anti-Stokes Raman scattering, second harmonic generation, third harmonic generation and third-order sum frequency generation, *Optics express*. 20: 9551-9557.
17. Débarre, D. , Supatto, W., Farge, E., Moulia, B., Schanne-Klein, M. C. and Beaurepaire E., 2004. Velocimetric third-harmonic generation microscopy: micrometer-scale quantification of morphogenetic movements in unstained embryos, *Opt. Lett*. 29: 2881-2883.
18. Gualda, E. J., Filippidis, G., Voglis, G., Vlachos, M., Fotakis, C. and Tavernarakis N., 2008. In vivo imaging of neurodegeneration in Caenorhabditis elegans by third harmonic generation microscopy. *J. Microsc.* 232: 270-275.
19. Tserevelakis, J. G., Filippidis, G., Krmpot, J. A., Vlachos, M., Fotakis, C. and Tavernarakis N., 2010. Imaging Caenorhabditis elegans embryogenesis by third harmonic generation microscopy. *Micron* 41: 444-447.
20. Tserevelakis, J. G., Filippidis, Megalou, V. E., Fotakis, C. and Tavernarakis N., 2011. Cell tracking in live Caenorhabditis elegans embryos via third harmonic generation imaging microscopy measurements. *J. Biomed. Opt.*16: 046019.
21. Bremer, S., 1974. The genetics of Caenorhabditis elegans, *Genetics* 77: 71-94.
22. Sulston, and Horvitz H. R., 1977. Post-embryonic cell lineages of nematode Caenorhabditis elegans. *Developmental Biology* 56: 110-156.

23. Sulston, E. J. , Schierenberg, E. , White, J. G. and Thomson, J. N., 1983. The embryonic cell lineage of the nematode Caenorhabditis elegans. *Developmental Biology* 100: 64-119.
24. *C. Elegans* Sequencing Consortium, 1998. 2012-2018. Genome sequence of *C. Elegans*: a platform for investigating biology. *Science* 282: 5396.
25. Kamath, S., R. and Ahringer, J., 2003. Genome-wide RNAi screening in Caenorhabditis elegans. *Methods* 30: 313-321.
26. Soukas, A. A. Kane, E. A., Carr, C. E., Melo, J. A., Ruvkun, G. 2009. Rictor/TORC2 regulates fat metabolism, feeding, growth and life span in Caenorhabditis elegans. *Genes Dev* 23: 496-511.
27. Ashrafi, K., Chang, F. Y., Watts, J. L., Fraser, A. G., Kamath, R. S., et al. 2003. Genome-wide RNAi analysis of Caenorhabditis elegans fat regulatory genes. *Nature* 421: 268-272.

Chapter 6. Adipose fat accumulation and quantification analysis in *C.elegans*.

6.1 Introduction

As it was explained in Chapter 5 lipid droplets give rise to THG signals in nematode *C. elegans*. We are able to use THG as a diagnostic tool to record fat deposition along the whole body of the animal. Particularly, we focused on the intestine region where fat accumulation is the main contributor of high THG signal. The fluctuation of fat accumulation is crucial information for the visualization and quantification of lipid content in adipose tissues at great accuracy and so as for studying aging. Fat accumulation of wild type animals characterized as lysosome function, can be examined by visualization of lipid droplets also in mutant animals. The decrease of lipid droplets in some mutants is attributed to impaired synthesis of unsaturated fats, since unsaturated fatty acids that are stored in lipid droplets and increased fatty acid oxidation to meet the energy demands of tissues [1,2]. On the other hand insulin signaling regulates longevity, aging and stress resistance in many organisms such as *C. elegans, Drosophila* and mice.

We show the results of visualization and quantification analysis of THG signal either of fat accumulation or lysosome mutants as detailed below. The capability of THG technique for lipid droplets detection was certified by imaging lipids in worms with mutations in fat accumulation and lysosome function. Purposely, we employed *fat-6;fat-7(wa36)* mutants that show decreased fat accumulation, and *daf-2(e1370)* mutants that show increased fat accumulation. We also examined *fat-6 (tm331)* mutants that are defective in lysosome formation, to test if THG is capable of faithfully reflecting alterations of fat content in this genetic background. *fat6;fat-7* and *fat-6* mutants seem to conjure less droplets up while *daf-2* mutants conjure significantly more droplets up. Last but not least, we monitored lipid accumulation at various stages throughout *C. elegans* lifespan whereby we determine whether fat storage changes with age. So as, we settle on lipids progressively accumulated until early adulthood, but lipid content progressively decreased until the end of life. The procedures of maintenance and *C. elegans* strains are mentioned in detail in previous chapter 5 for wild type and mutant animals.

We propose THG to be a powerful, easily acquired technique to detect lipids in all organisms, investigate cellular and molecular mechanisms controlling fat storage and metabolism. The results of measurements are given below.

6.2 Visualization of lipid depositions in fat and lysosome mutants during *C. elegans* lifespan.

Initially, we used *daf-2* (e-1370) mutants. Mutations in *daf-2* gene encoding the insulin/IGF receptor increases lipid deposition compared to wild type worms [3]. Specifically, daf-2 mutants have more fat storage in contrast with wild type animals [4,5,6,7,]. Disorders in Δ9 fatty acid decrease the fat content in intestinal cells and provide fat-6 and fat-6;fat7 (fat-6;fat-7 double mutant) mutants [8,9]. We found that daf-2 mutants show an increased fat accumulation while fat-6;fat-7 double and fat-6 mutants showed reduced fat accumulation. In the second ones, the main reason is the lack of enzymes which decreases lipid synthesis as well as the levels of complex lipids like cholesterol esters, phospholipids and triacylglycerides. Furthermore, the insulin resistance that provide, can easily affect fat storage respectively.

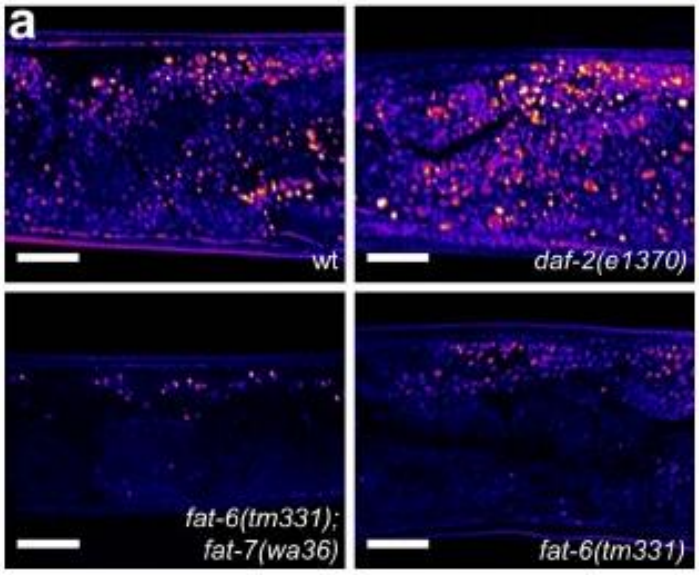

Figure 6.2.1: a) THG visualization of lipid droplets in wild type and mutant animals. Mutant daf-2 has more lipid content than wild type worms. fat-6;fat-7 double mutant and fat-6 mutant have fewer respectively. Scale bars in images denote 20μm.

As a result, we are able to use THG for monitoring alterations in lipid depositions in *C. elegans.*

A question with great importance has been brought to light. Whether fat storage changes with aging and THG monitoring could be cope this procedure. The animals were monitor in different developmental stages starting from the first (L1) and last (L4) larval stage followed by adult

animals (Days of 1,5,10 and 15). In Figures 6.2.2(a-d) it is depicted the progressive fat accumulation from early life stage (larval stage L1) until early adulthood (Day 5) and in Figure 6.2.2e),f) the respective progressive loss of fat content in Days 10 and 15 of adulthood.

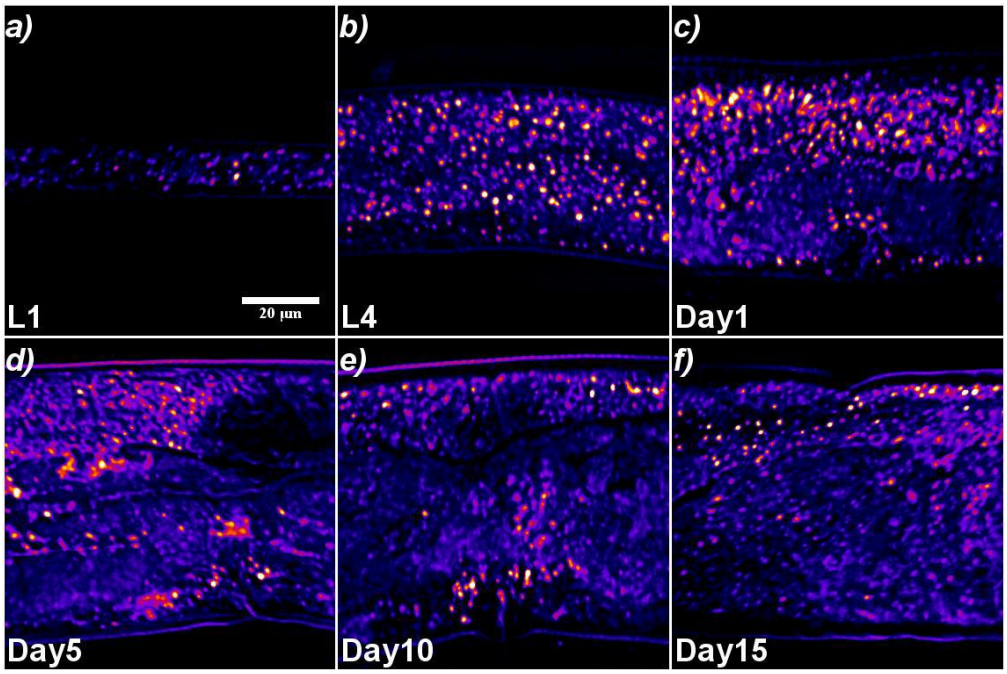

Figure 6.2.2: Configuration of lipid deposition via THG technique during developmental stages in *C. elegans*.Larval stages a) L1 and b) L4. Days c) 1, d) 5, e) 10, f) 15 of adulthood. It is shown increased fat accumulation in early life stage until Day 5 of adulthood and significant fat reduction in Day 10 and 15.

6.3 Quantification of lipid particles in *C. elegans*.

During THG imaging has been observed regions of animal that generate high levels of nonlinear signal primarily corresponding to lipid particles. As a consequence, lipid particles of these regions have to be isolated and separated in order to achieve quantification of the related signal. We set a threshold in slice images after normalizing them. Processing of imaging and threshold performing were carried out by using Image J. The setup provided a 600x600 pixel THG scan and 20 scans were averaged for each final image. For further improvement in picture quality, a series of 2D optical section was acquired at 2μm intervals in z stack and projected onto a single plane. 8 bit normalized slice images were used in Image J and afterwards was applied constant threshold value so as only the 20% of high THG signal was recorded. The quantification included the use of Analyze Particles function of Image J generating a stack of binary images which in combination with thresholding procedure represented the lipid droplets in the intestine of *C. elegans.* The lower THG signals arising from other inhomogeneous structures were eliminated. The lipid content calculation included the total area of the detected regions for all sequential optical planes covering the sample depth. The number of worms that was examined for each genetic background and developmental stage was at least 10 and the mean pixel intensities were calculated by averaging the values obtained for each image after setting the threshold by Image J. Subsequently, we calculate the total sum of the detected area's pixels which revealed the total lipid content within the examined part of the intestine and lastly, total lipid particle area measurements of different samples were compared by one-way ANOVA and Tukey HSD *post hoc* tests (SPSS, IBM Corp., USA).

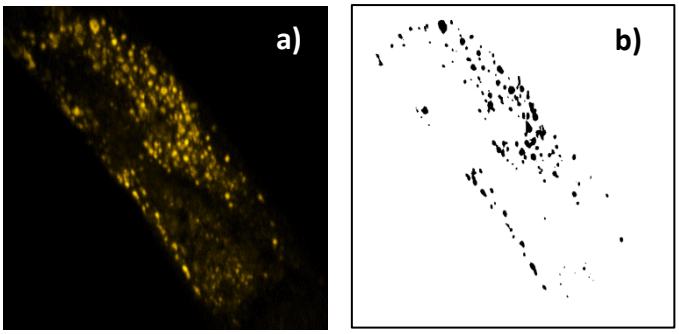

Figure 6.3.1: a) 4-day-old wild type (N2) *C. elegans* where lipids of the intestine region are depicted with THG signal. b) Binary central slice of THG that corresponds to 4-day-old animal.

Quantification of lipid deposition in wild type and mutants.

As it was mentioned before, there were used wild type and mutants *C. elegans* . The areas of lipid particles in different worm populations were compared by one-way ANOVA. It is denoted that daf-2 mutants had more lipid droplets (P< 0.001) in contrast with fat-6;fat-7 and fat-6 mutants where Tukey *post hoc* tests indicated that there was a significant reduction of lipid content (P< 0.001). The number of the examined animals was 10 for each mutant and wild type population. This quantified result confirmed the initial issue that daf-2 mutants showed an increased fat accumulation than wild type and mutants fat-6;fat-7 and fat-6 showed a reduced accumulation. Figure 6.3.2.

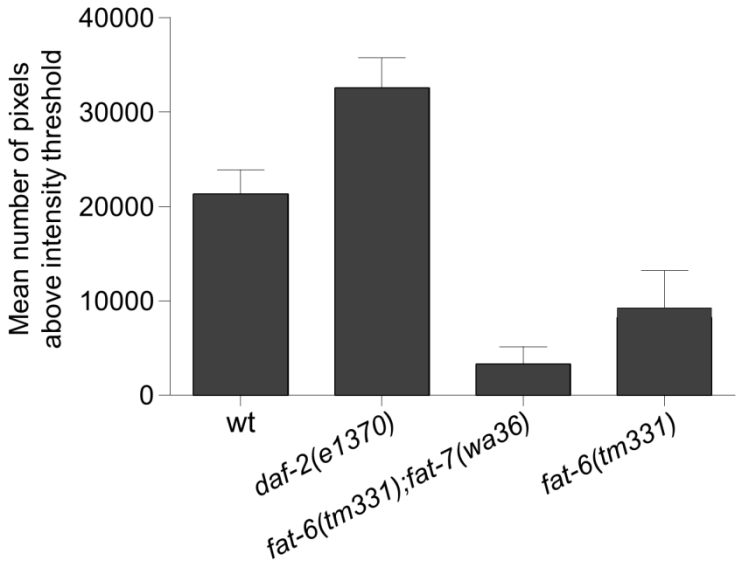

Figure 6.3.2: Quantification of THG signal in the intestine region of wild type and mutant *C. elegans*. Sample number N=10.

At least 10 worms were examined for each genetic background and developmental stage. We can easily notice from the diagram that mean pixel intensities were calculated by averaging values obtained for each image after thresholding to quantify the obtained THG signal. Mutants daf-2 seem to have a great percentage of fat accumulation followed by fat-6 mutants as compared with fat-6;fat-7 mutants which conjure up less .All types of mutants compared with wild type in the level of mean number of pixels above a constant intensity threshold.

Quantification of lipid droplets during C. elegans lifespan.

To quantify how fat accumulation reacts or changes with aging, we monitored lipid content in the intestine of the worms at various time points during lifespan. At first (L1) and last (L4) larval stages and at five days across adulthood until their death (Day 1, 5, 10, 15) as it is shown in Figure 6.3.2. We found that fat accumulated progressively from early life (larval stage L1) until early adulthood (Day 5), but then the reverse phenomenon occurred of progressive loss of deposited fat (Days 10 and 15, Figure 6.3.2). A one-way ANOVA indicated a significant overall effect of the amount of fat deposition during worm lifespan, as well as Tukey HSD post hoc tests indicated that more fat was deposited at the L4 larval stage ($P<0.001$, L4), the first ($P<0.001$, Day 1) and fifth ($P<0.001$, Day 5) day of adulthood. It was observed that lipid droplets in worms initially increased until their early adulthood followed by a reduction in late adulthood. Such accumulation of fat could be correlated with that in humans.

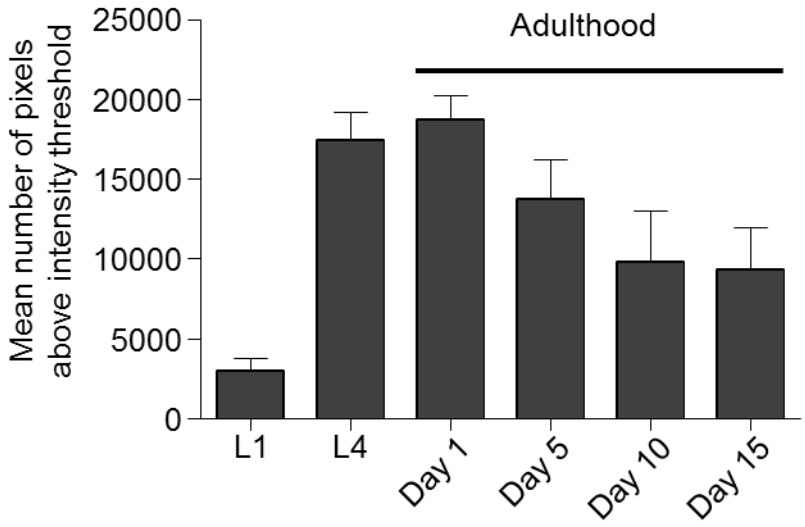

Figure 6.3.3: Quantification of THG imaging of lipid droplets at specific developmental stages (L1 and L4 larval stages) and during adulthood (at day 1,5,10,15).

Figure 6.3.4: Aging process in humans

Thus, THG can be used to quantitatively measure fat deposition across the lifespan of the worm and thereby provide insight into the levels of body fat in humans during aging. Furthermore it comprises a reliable new diagnostic tool to measure fat levels in the body of model organisms and tissues. THG is one of the most capable techniques for detecting lipid depositions by imaging *C. elegans* wild type animals and mutants with altered fat storage profiles.

Chapter References

1. Flowers, T, M, Ntambi, M, J, 2008. Role of stearoyl – coenzyme A desaturase in regulating lipid metabolism. *Current opinion in lipidology* . 16(3):248-256.
2. Castro, C., Sar, F, Shaw, R, W, Mishima, M., Miska, A., E. and Griffin, L., J, 2012. A metabolomic strategy defines the regulation of lipid content and global metabolism by Delta9 desaturases in Caenorhabditis elegans. *BMC genomics*. 13:36.
3. Watts, L., J. Fat synthesis and adiposity regulation in Caenorhabditis elegans . 2009. *Trends Endocrinol Metab* . 20:58-65.
4. Ashrafi, K., Chang, Y., F., Watts, L., J. , Fraser, G., A., Kamath, S., R., Ahringer, J. and Ruvkun, G. 2003. Genome-wide RNAi analysis of Caenorhanditis elegans fat regulatory genes. *Nature* .421:268-272.
5. Yen, K., Le, T., T., Bansal, A., Narasimhan, D., S., Cheng, X., S. and Tissenbaum, A., H., 2010. A comparative study of fat storage quantitation in Caenorhabditis elegans using label and label free methods. *PloS one* .5(9).

6. O' Rourke, J., E., Soukas, A.,A., Carr, E.,C. and Ruvkun, G.2009. *C. Elegans* major fats are stored in vesicles distinct from lysosome-related organelles. *Cell metabolism* .10:430-435.
7. Kimura, D., K., Tissenbaum, A., H., Liu, Y. and Ruvkun, G. 1997. daf-2 an insulin receptor-like gene that regulates longevity and diapause in Caenorhabditis elegans. *Science*. 277:942-946.
8. Brock, T., J., Browse, J., Watts, J.,L. 2006. Genetic regulation of unsaturated fatty acid composition in C.elegans. *PloS Genet* 2:e108.
9. Hermann, G.,J., Schroeder, L.,K., Hieb, G.,A., Kershner, A.,M., Rabbits, B.,M., et.al.2005. Genetic analysis of lysosomal trafficking in Caenorhanditis elegans. Mol. Biol. Cell.16:3273-3288.

Chapter 7. Imaging and quantifying ectopic fat accumulation in muscular region of *C. elegans*.

7.1 Introduction

As THG imaging technique is the most appropriate technique for detecting lipid body structures in tissues and cells [1,2], it is also important to use it for identifying structures that are localized in other regions of body worm *C. elegans***.** Previously in Chapter 6 we visualized successfully the intestinal lipid droplets which are parts of the adipose tissue in *C. elegans* while TPEF was performed using labels in order to verify the success of THG imaging of lipids [3,4]. It is significant to mention that THG is capable of revealing the morphology of unstained tissues [5] and for monitoring and individuating the different developmental stages in wild type and mutant animals [6,7]. The fact that we are able to get information for development in different ages of the worm, gives us additionally a chance for correlating aging and lipid accumulation in non-adipose tissues.

Initially, we used THG microscopy as a diagnostic tool to operate, detect and quantify lipid content of ectopic fat in non-adipose tissue and particularly on pharyngeal muscles. We performed simultaneously SHG and THG for monitoring, three-dimensional imaging and furthermore analysis of the muscular areas and the lipid droplets accumulation. The existence and anatomical information about the structure of the muscles are provided by SHG imaging which is also used to certify the efficiency of THG imaging of stained lipids with various labels [8]. Overburdened adipose tissue causes lipids and fat accumulation also in non-adipose tissues such as skeletal muscles and pharyngeal muscles, known as ectopic fat accumulation which is involved in the pathogenesis of metabolic syndrome [9]. It is believed that it contributes to organ dysfunction, impaired muscle strength and insulin resistance in skeletal muscles [10]. This is the reason why we paid attention in lipid droplets of muscular areas of *C. elegans* during various developmental stages or during aging.

In addition, we show how fat depositions is accrued with age in non-adipose tissues such as body wall muscles, pharyngeal muscles of *C. elegans* and also how this can be influenced in some mutant animals.

7.2 Identification of muscular lipid content in *C. elegans* .

THG microscopy in previous studies confirmed the existence of lipid droplets in adipose tissue of *C. elegans* and from now on we can use it as a diagnostic tool for visualizing these structures with great accuracy in non-adipose tissue of the animal even in non-labelled samples. Non-adipose tissue known also as ectopic fat can be found among normal cells of senescent tissues and in multiple body regions of the worm including skeletal and pharyngeal muscles [11]. We choose for monitoring lipid content the head region where is full of muscles that originate strong SHG signal.

THG and SHG imaging are reliable techniques for getting anatomic features of the whole body of 1-day-old adult wild type *C. elegans.* This can be achieved by performing simultaneously THG and SHG measurements. As it is depicted below THG reveals mostly morphological information such as shape, contour and internal structures of the animal. On the other hand SHG reveals anatomical information for the body wall muscles, the two pharyngeal bulbs, the striated muscles in the mid-body region, the vulva and the muscles located in the posterior part of the worm.

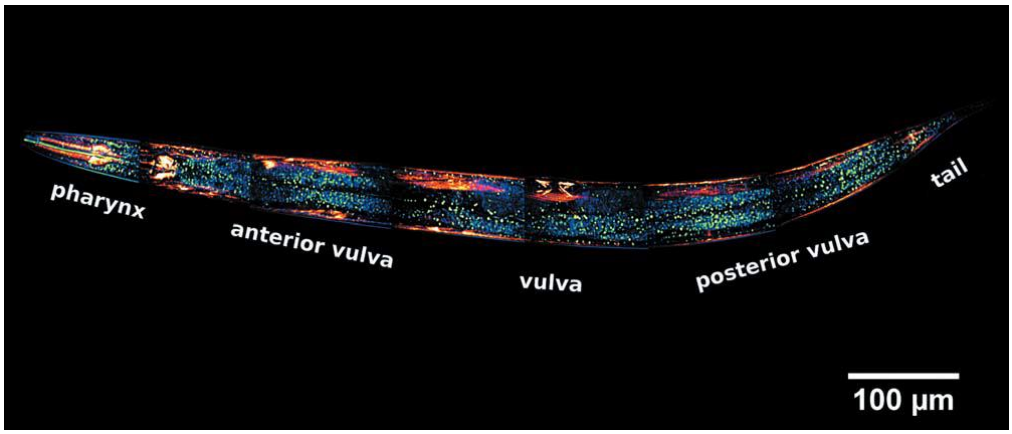

Figure 7.2.1: Imaging the whole body of 1-day old adult wild type *C. elegans.* Visualization of the intracellular structures - lipids, lumen, cuticle - by THG (*green blue*) and of the musculature of the animal by SHG (*red hot*).

First of all, we have to make clear that THG signal originates from lipid droplets and not from other cellular structures of the worm. For this reason we used Nile Red dye in the head region to specifically stain lipid droplets of the animal (Chapter 5). We observed a significant colocalization of THG and TPEF signal, which were simultaneously performed on the pharynx of *C. elegans*. For our measurements the area of pharynx was selected because between the two bulbs there is no contribution of the intestinal cells, thus it is eliminated from the lipid

quantification. The multi-modal information that is obtained by the simultaneous non-linear imaging is depicted in Figure 7.2.2.

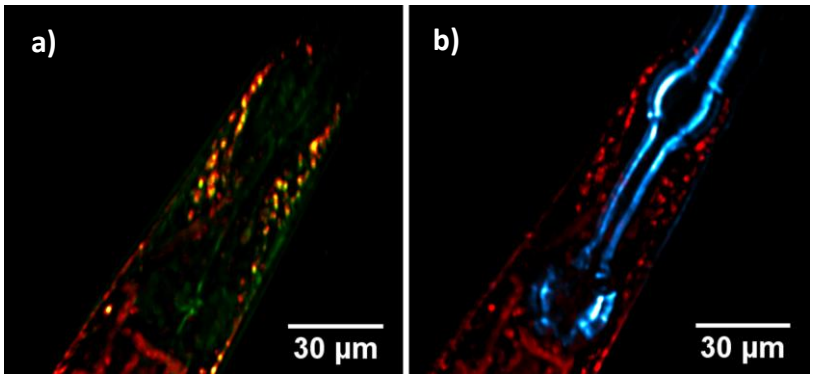

Figure 7.2.2: The three-color images of the head area of a 1-day old stained adult *C. elegans*. (a) THG (green) arises from internal head structures (mostly lipids), TPEF (red) emanating from the lipids stained with Nile Red, (b) SHG (cyan hot) originating from the musculature of the head region (pharyngeal and body-wall muscles) and TPEF (red) coming from the stained lipids.

We pointed out high THG signal which came from the internal lipid structures corroborating the ectopic fat accumulation on the pharyngeal muscles by colocalization measurements where Nile Red stained lipid droplets in fixed animals occurring TPEF signal (Figure 7.2.2 a). It is shown that the fluorescence of lipid structures stained by Nile Red (red) were colocalized with THG signals (green) and as a result we got the colocalized structures (*yellow*) (Figure 7.2.2 a) that represent lipid droplets and furthermore the ectopic fat in the head region of *C. elegans*. The pharyngeal and body wall muscles are depicted by SHG imaging (Figure 7.2.2 b). Another region that has been brought into focus was the middle body and tail region where there is a large amount of muscles that were tagged with GFP (Green Fluorescent Protein). Figure 7.2.3 and 7.2.4 give the recorded images of 9-days adult *C. elegans* where THG is depicted with blue colour representing ectopic lipid droplets and TPEF is depicted with green colour representing the muscles of the region. The animals were treated according to the methods described in the following section.

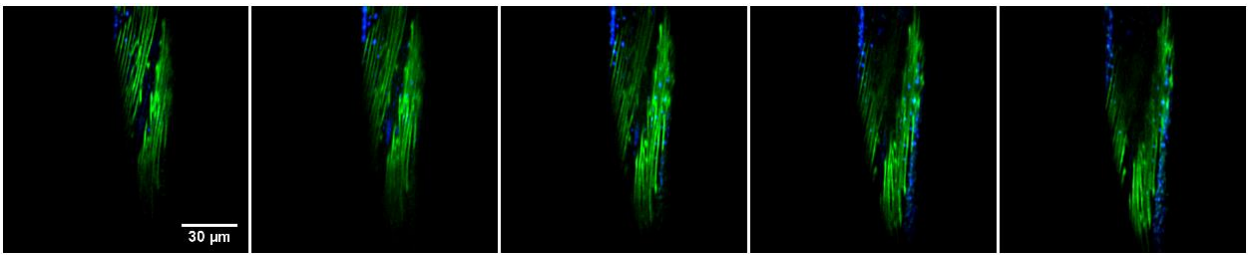

Figure 7.2.3: Configuration of ectopic fat content in the middle region of wild type animal at day 9 of adulthood. The two dimensional sequences are divided by 2µm. The multi-modal

image depicts TPEF (green) arising from the muscles and THG (blue) signals arising from the lipids.

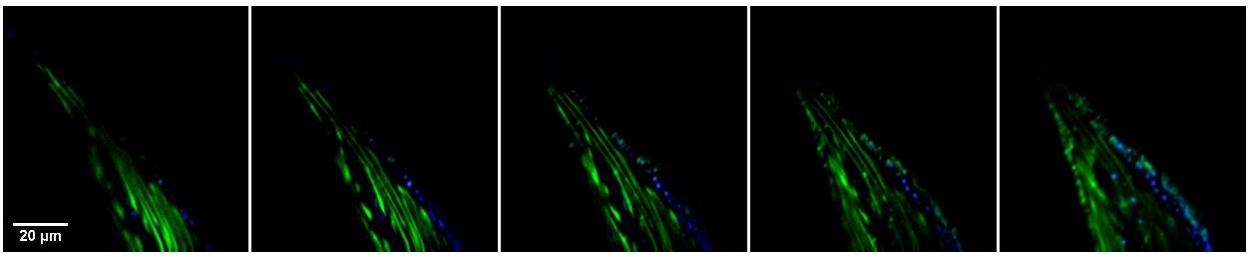

Figure 7.2.4: Configuration of ectopic fat content in the region of tail in wild type animal at day 9 of adulthood. The two dimensional sequences are divided by 2µm. The multi-modal image depicts TPEF (green) arising from the muscles and THG (blue) signals arising from the lipids.

Now we ensure the fact that these components indicate the ectopic fat in the pharyngeal muscles of the animal and by extension indicate it in the head region, the middle body and the tail, areas where exist a large amount of muscles.

C. elegans strains and maintenance.

The procedures that were followed for *C. elegans* maintenance were equivalent to them in the previous chapter.

Lipid staining.

The lipid staining has been carried out in the same way as in the previous chapter. Worms were fixed for 5 min in 3mL cold (-20 ^{o}C) methanol. Subsequently, 2mL of PBTw (PBS with 0.1% Tween-20) were added and tubes were centrifigured for 2 min at 3000 rpm to remove the supernatant. After that worms were washed twice in PBTw. Following fixation worms were stained for 20min in 10 mM Nile Red (Sigma-Aldrich Corp.), added from a stock solution of 50mM Nile Red diluted in 100% ethanol. For the second and third generation imaging worms were collected with M9 isotonic buffer (22 mM KH_2PO_4 (Merck cat. no. 1.04873.1000), 42 mM Na_2HPO_4 (Merck cat. no. 1.06586.0500), 85 mM NaCl (Merck cat. no. 1.06404.1000) and 1 mM

$MgSO_4$ (Sigma cat. no. M-7506). Dissolve 3g KH_2PO_4, 6g Na_2HPO_4, 5g NaCl and 1m: 1 M $MgSO_4$ in 1 L distilled water. Autoclave and keep it refrigerated). Then, worms were washed several times with M9 buffer to remove bacteria. Finally, the worms were immobilized with 10mM sodium azide buffer at final concentration. The immobilization of the worms is examined microscopically. We used IR28: N2; *Is001* [p_{myo-3}MYO-3::GFP] to monitor body wall muscle cells.

Transgenic animals that expressed the myosin heavy chain, MYO-3, had been tagged with GFP in body wall muscles where lipid droplets were detected via THG in the striated body wall muscle cells in the head, the middle body and the tail of *wild type* animals at day 9 of adulthood.

Quantification of ectopic fat accumulation in wild type animals.

THG microscopy is capable of detecting the lipid content and providing images of high resolution, but also it is useful for quantification measurements. The collected THG signal quantification determines numerically the ectopic fat accumulation and also the fat distribution during various developmental stages. Previous studies have shown changes that occur in fat distribution for elderly animals could cause lipotoxicity effects, contributing to the disruption of tissue function during aging [12]. Furthermore, is possible free fatty acid (FFAs) or their metabolites triggering cell death or oxidative stress damaging cellular function [13]. Additionally, it has been reported a significant correlation between ectopic fat accumulation and the process of aging.

Quantification is performed on the lipids of the middle 8 layers so that intestinal and epidermal lipids are eliminated. This is important because THG signal that derived from adipose tissue had to be excluded in order to get a clear signal of lipids from the ectopic fat. In this region coexist strong muscles that emanate SHG signal providing the area that lacks of adipose tissue. The regions that generated high levels of nonlinear signal, where lipids are full, were detected and then isolated.

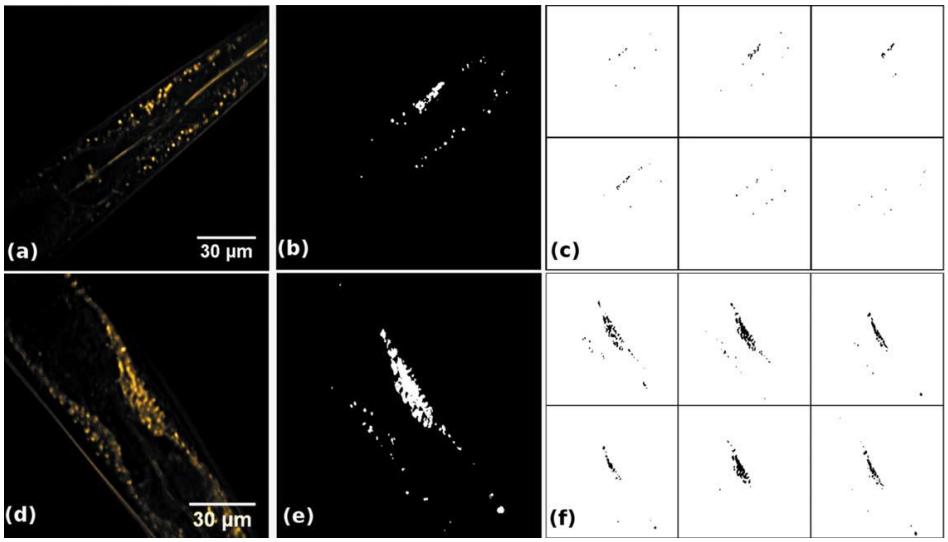

Figure 7.2.5: a), d) 1-day-old and 9-day-old wild type (N2) *C. elegans.* b), e) z-projection of binary thresholded slices of 1-day-old and 9-day-old animals. c) and f) six binary central slices of THG that corresponds to 1-day-old and 9-day-old animals respectively.

All the samples have been imaged under constant irradiation conditions. We used ImageJ to get a threshold on the normalized slice images that we obtained. The normalized 8-bit images were thresholded with a constant value and only the highest 25% of THG signals were included in quantification measurements. Signal from contour, mouth or lumen had to be excluded so as the generated binary images represented strictly only lipids droplets in the muscles. We calculate the total pixel area of detected regions for all optical planes, covering the total sample volume. Quantification actualized in the pharyngeal region of 1-day-old and 9-day-old wild type (N2) *C. elegans* respectively. Figure 7.2.5 a) and d) represents the recorded THG images of the examined region, while their z-projection is given in Figures 7.2.5 b), e). Lastly, in Figures 7.2.5c) and f) are depicted six binary central slices of THG which got a constant threshold and represents 1-day-old and 9-day-old wild type animals. The total lipid content within the examined part of the pharynx region is calculated with the total sum of the detected areas in pixels and the total lipid particle area measurements of the two different samples are compared by one sample t-test (SPSS, IBM Corp.).

Ectopic fat of 1-day and 9-day old animal as a total value is calculated and averaged over a number of 18 animals for each age. The lipids that were calculated were those between the two bulbs of the pharynx. Below, is given a representation of the mean total lipid content area in the head muscles of wild type animals.

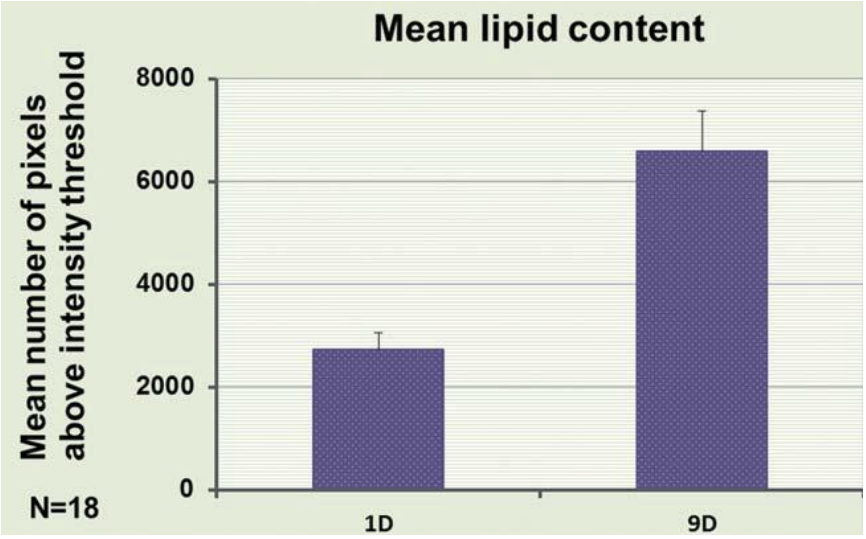

Figure 7.2.6: Quantification of the mean total lipid area for 1-day-old and 9-day-old wild type (N2) animals. The normalization has been performed in 18 animals upon the body size.

The information that we derived from the graph is the increase in the ectopic fat content in pharyngeal muscles of wild type animals along the age progress of the animals. There is a significant difference in statistical measurements ($P<0.005$). Keeping that in mind, we examined if physiology and metabolic rate of *C. elegans* could be affected from temperature.

We choose three different temperatures at 1-day and 4-days old animals and we notice that ectopic fat content changes similarly during growing temperature with a peak at 25^{o}C for 1-day old animals and a peak at 20^{o}C for 4-days old animals.

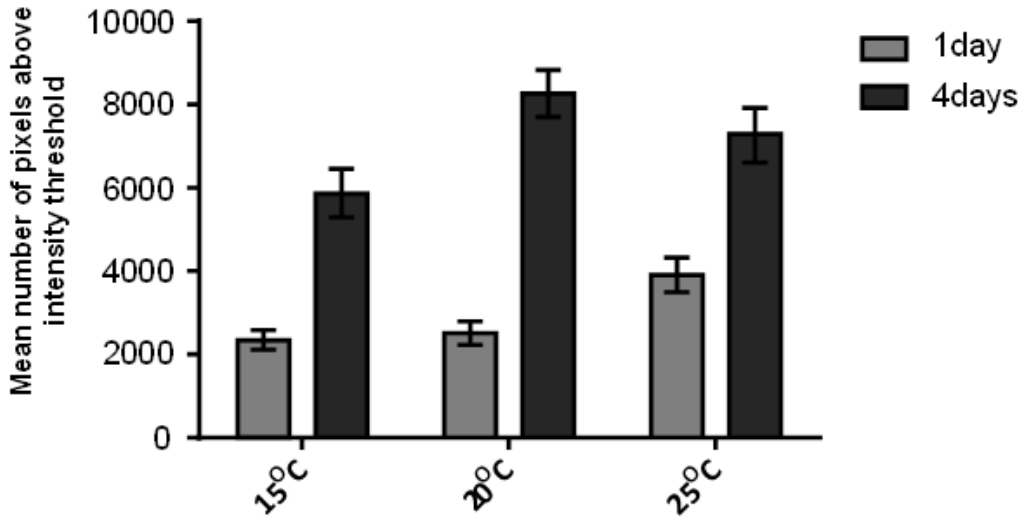

Figure 7.2.7: Wild type animals rose at 15^{o}C, 20^{o}C and 25^{o}C in 1 day and 4 days display similar ectopic fat levels.

Although temperature influences *C. elegans* physiology and metabolic rate, lipids expand ectopically in a temperature-independent manner. Age-matched animals were raised at different growing temperatures (15^{o}C, 20^{o}C and 25^{o}C) display similar ectopic fat levels throughout life.

By exploiting THG modality not only as a non-destructive and label-free diagnostic tool but also as a quantification tool, we are able to visualize and quantify ectopic fat depositions in lipid biology studies. With the simultaneous contribution of SHG we can get anatomical and morphological information for the musculature. We continue beneath our work with some mutant animals for confirmation and further ascertainment of our obtained results

7.3 Ectopic fat distribution in mutants *C. elegans.*

***C. elegans* strains and culture methods.**

We followed standard procedures for *C. elegans* strain maintenance. Nematode rearing temperature was kept at 20^{o}C, unless noted otherwise. The following strains were used in this study: N2: wild-type Bristol isolate, CB1189: *unc-51(e1189)V*, DA465: *eat-2(ad465)II*, *lgg-2(tm5755)IV*, *lipl-4(tm4417)V*.

Molecular cloning.

To generate the p$_{hlh-17}$GFP reporter construct, we fused a *Sal*I/*Kpn*I fragment, containing the sequence of *hlh-17* promoter, amplified from *C.* elegans genomic DNA using the primers 5'ACGCGTCGACATGACGGAGTTGAGGCCAAAATCC3'and5' CGGGGTACCGACTGGGGTGTAAGTGAATGAGAGAGGA3', at the amino (N) terminus of GFP, in the pPD95.77 plasmid vector. Thep$_{hlh-17}$GFP reporter construct was co-injected with pRF4 (contains the *rol-6(su1006)* dominant transformation marker) into the gonads of wild-type animals. For engineering the *hlh-30* RNAi construct, gene-specific fragments of interest were obtained by PCR amplification directly from *C. elegans* genomic DNA using the following sets of

primers 5'TTGACATTTCCAACGAGACGC3'and 5'TGCTCGTCCCTAGAATTCACA3'.
The fat staining with Nile red has been described previously.

In Chapter 6 we found that adipose fat increases during several developmental stages, followed by some reduction during adulthood [14]. On the other hand in this study was determined an increase of ectopic fat that is linked with age [15]. Now, we go a little bit further to analyze some types of mutation in *C. elegans* and how these react along lifespan. Caloric restriction is very important parameter in aging of the worms. It causes a significant delay during time in species relieving ectopic fat levels and under this condition autophagy is taken place. *C. elegans* mutation that is responsible for this function is *eat-2(ad465).* It reduces the pumping rate of the animal [16] and it regulates the caloric restriction on ectopic fat deposition [17,18]. *eat-2(ad465)* mutants in comparison with wild type animals seem to have a decrease in ectopic fat storage in the pharyngeal muscles. As it was mentioned before, the area that was chosen was that between two bulbs of *C. elegans* in both types of 1-day, 9-day and 12-day old animals.

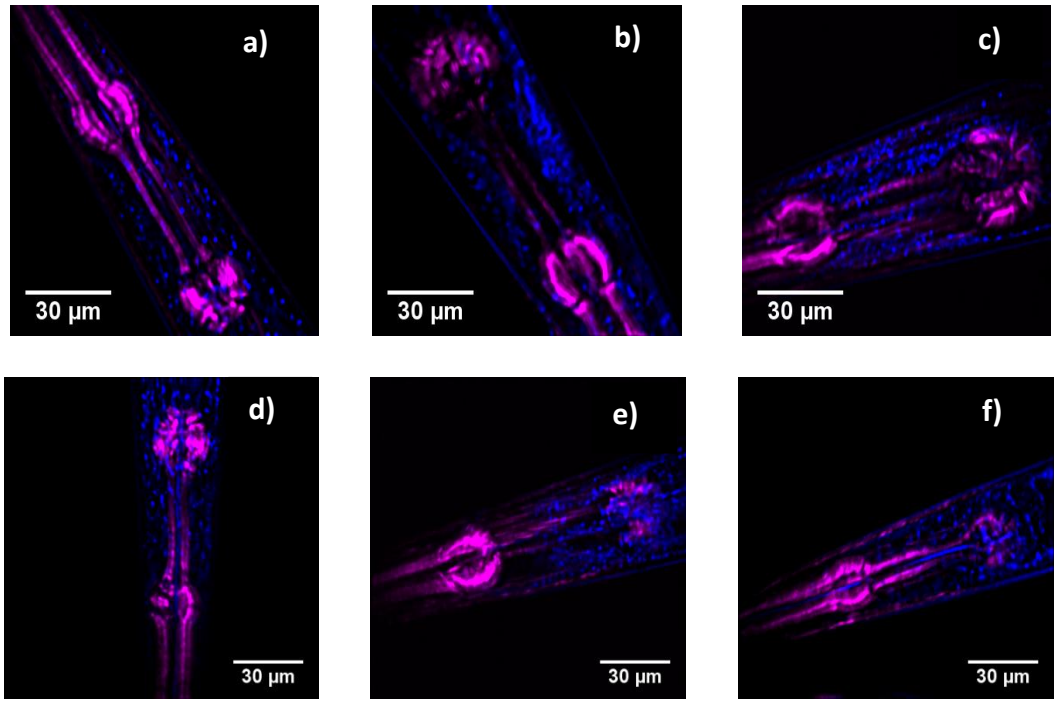

Figure 7.3.1: Nonlinear modalities reveal ectopic fat distribution in wild type at day a) 1, b) 9 and c) 12 and *eat-2(ad465)* mutants at day d) 1, e) 9 and f) 12 respectively. THG (*blue)* shows ectopic lipid droplets and SHG (*magenta*) the musculature. All images are z-projected to maximum intensity three-dimensional slices divided by 2μm.

We recorded the ectopic fat accumulation in wild type and mutant *eat-2(ad465)* which induced a small increase in 1-day-old animals followed by elder animals of 9 and 12-days where there was a considerable reduction of ectopic lipid droplets. This result is given below by a quantification diagram.

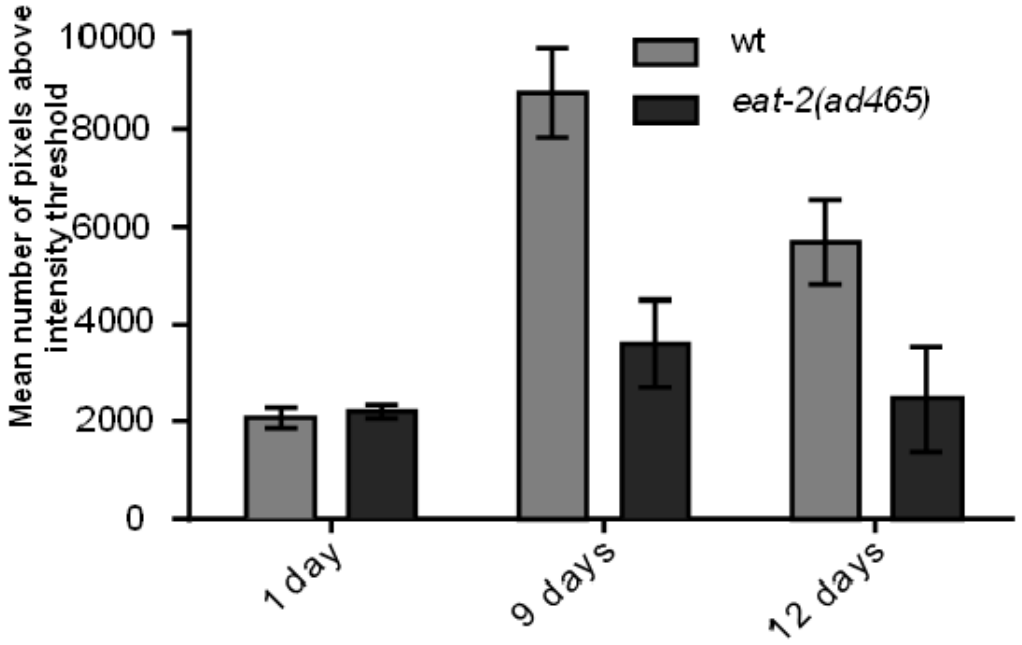

Figure 7.3.2: Quantification diagram of *wild type* and *eat-2(ad465)* during aging.

The other mutant category that displayed and important role was *hlh-30(RNAi)* which helps the expression of several lysosomal and autophagy genes because is the homolog of the basic helix-loop-helix Transcription Factor EB (TFEB). This factor regulates the catabolic process of autophagy and it is required for the increase of the longevity of *eat-2(ad465)* mutants [19,20]. It is clear that both *wt* and *hlh-30(RNAi)* have more ectopic fat between 1 and 9-days, while *eat-2(ad465)* indicates not so high level as those two previous animals in the 9-days age.

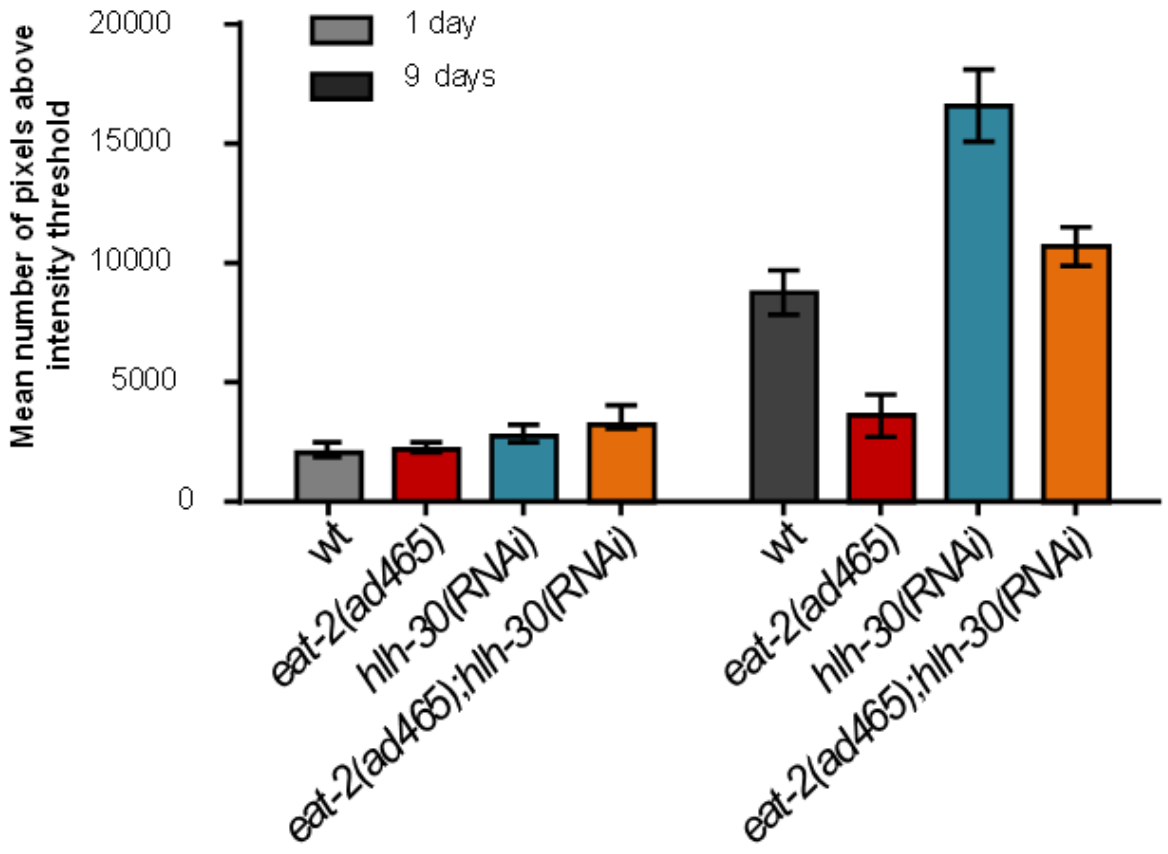

Figure 7.3.3: Quantification of *wild type*, *eat-2(ad465)* and *hlh-30(RNAi)* mutants at day 1 and 9 of lifespan.

As ectopic fat deposition is age-dependent we noticed that the contribution of *hlh-30(RNAi)* regulated the excess or lack of lipid content. Specifically, we knocked down *hlh-30(RNAi)* in *wild type* and *eat-2(ad465)* animals and the result was an excess of ectopic lipid accumulation caused by *hlh-30(RNAi)* depletion (Figure 7.3.3).

Now we examine *lgg-1* mutant which encode the homolog of the mammalian LC3. The diagram below reveals that knockdown of *lgg-1* mutant results increase in lipid deposition in pharyngeal muscles of *eat-2(ad465)* animals, while suppression of autophagy did not cause any changes in ectopic fat accumulation in wild type animals during aging. Under normal conditions autophagy affects ectopic fat distribution but *hlh-30(RNAi)* mutant is the one that moderates the independence of it in wild type nematode. Ectopic fat regulation except from caloric restriction can be affected from lysosomal activity depended on several lysosomal genes that modulate fat content due to lysosomal acid lipases that catabolize lipid droplets [21].

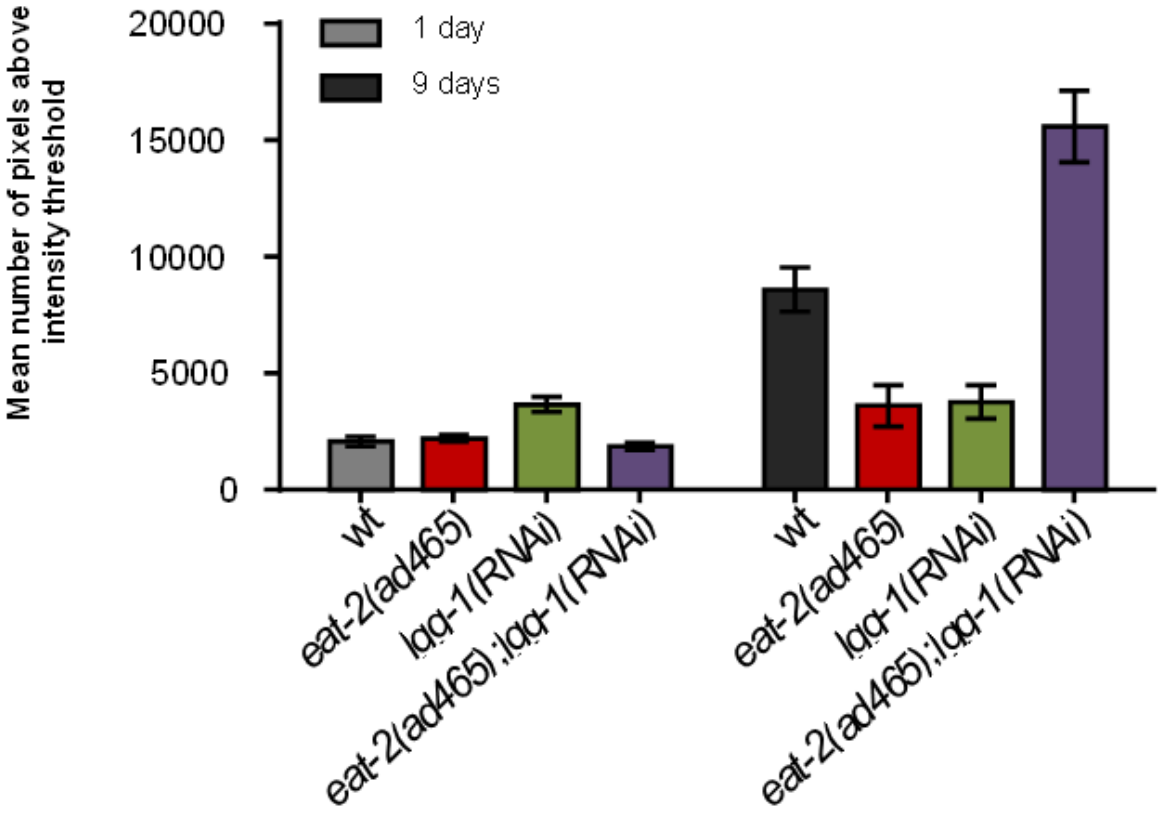

Figure 7.3.4: Statistical diagram of quantifying nonlinear modalities for *wild type*, *eat-2(ad465)* and *lgg-1* mutants.

For this reason we monitored fat accumulation in pharyngeal muscles of *lipl-4(tm4417)* mutants. Lipid metabolism is modulated by these mutants and moreover regulates lifespan extension while they consisted of lysosomal triglyceride lipases [22]. From quantification diagram we notice that ectopic fat distribution is equivalent to lack of *lipl-4(tm4417)* which means that we do not have any increase in fat content along lifespan.

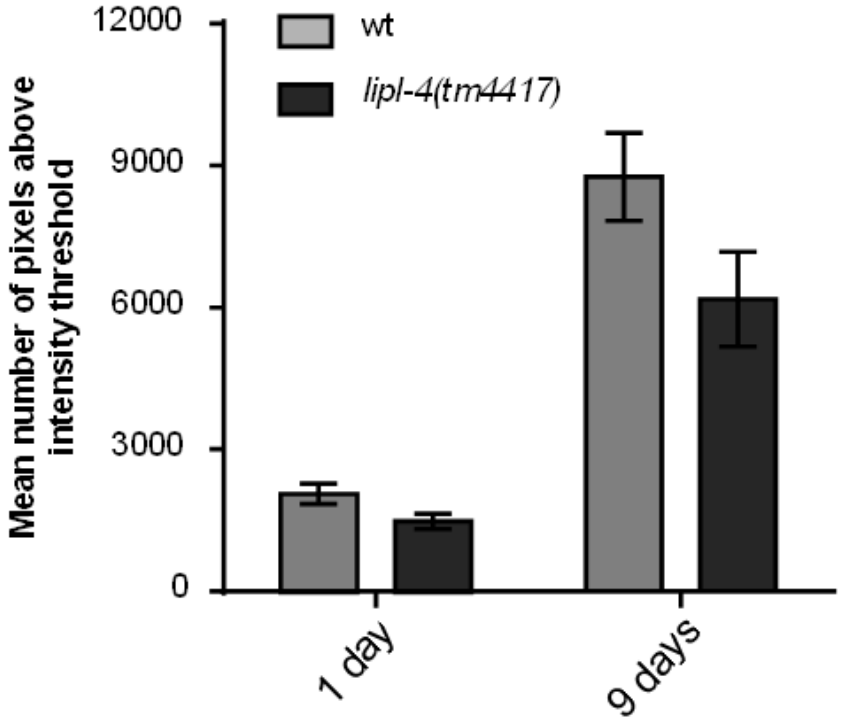

Figure 7.3.5: Quantification diagram at 1day and 9 days for *wild type* and *lipl-4(tm4417)* mutants.

In each quantification measurements the number of wild type and mutant animals were 12 (n=12). We see that the role of mutants in caloric and lysosomal function is critical due to the fact that they ordinate lipid metabolism when autophagy is not implicated in the regulation of ectopic lipid distribution.

As a consequence, by employing non-linear phenomena such as Second and Third Harmonic Generation (SHG and THG) simultaneously, we obtain fast and complementary information

concerning lipid accumulation on the muscles of wild type and mutant *C. elegans* in different developmental stages and temperatures. Additionally, THG microscopy was used as a quantitative tool to record the lipid content focusing on the pharyngeal muscles of the animal. Simultaneously, SHG microscopy provided anatomical information on the muscular structure of the specimens. Our results suggests a correlation of ectopic fat with the process of aging and can contribute to the unrolling of the correlation between lipotoxicity and aging but mainly to the validation of SHG and THG microscopy modalities as new, fast, non-invasive tools to localize and quantify selectively lipid droplets formation.

Concluding THG modality can be used as a new, label free, non destructive, high resolution technique, alternative to fluorescence and dye-based approaches, for lipid biology research. This imaging modality has the potential to provide novel insights for imaging and precise quantification of adipose and ectopic fat distribution of various biological samples during aging procedures.

Chapter References

1. Debarre, D. et al., 2006. Imaging lipid bodies in cells and tissues using third-harmonic generation microscopy. *Nat. Meth*., 3:47-53.
2. Zimmerley, M., Mahou, P., Debarre, D., Schanne-Klein, M. –C. & Beaurepaire, E., 2013. Probing Ordered Lipid Assemblies with Polarized Third-Harmonic-Generation Microscopy. *Physical Review* X, 3:011002.
3. Tserevelakis, G. et al., 2014. Label-Free Imaging of Lipid Depositions in *C.elegans* Using Third-Harmonic Generation Microscopy. *PLoS ONE*, 9:e84431.
4. Tserevelakis, G. et al., 2014. Label-Free Imaging of Lipid Depositions in *C.elegans* Using Third-Harmonic Generation Microscopy. *PLoS ONE*, 9:e84431.
5. Oron, D. et al., 2004. Depth-resolved structural imaging by third-harmonic generation microscopy. *Journal of Structural Biology*, 147:3-11.
6. Aviles-Espinosa, R. et al., 2010. Third-harmonic generation for the study of Caenorhabditis elegans embryogenesis. *BIOMEDO*, 15:046020-046020-046027.
7. Tserevelakis, J., G. et al., 2010. Imaging Caenorhabditis elegans embryogenesis by third-harmonic generation microscopy. *Micron*, 41:444-447.

8. Tserevelakis, G. et al., 2014. Label-Free Imaging of Lipid Depositions in *C. elegans* Using Third-Harmonic Generation Microscopy. *PLoS ONE*, 9:e84431.
9. Le Lay, S. & Dugail, I. 2009. Connecting lipid droplet biology and the metabolic syndrome. *Progress in lipid research*, 48:191-195.
10. Kuk, J., L., Saunders, T., J., Davidson, L., E. & Ross, R., 2009. Age-related changes in total and regional fat distribution. *Aging research reviews*, 8:339-348.
11. Youm, Y., H. et al., 2010. Thiazolidinedione treatment and constitutive-PPARgamma activation induces ectopic adipogenesis and promotes age-related thymic involution. *Aging cell*, 9:478-489.
12. Hemdon, L., A., Schmeinssner, P., J. Dudaronek, J., M., Brown, P., A., Listner, K., M., Sakano, Y., Paupard, M., C., Hall, D., H., Driscoll, M., 2002. Stochastic and genetic factors influence tissue-specific decline in aging C. elegans. *Nature*, 419:808-814.
13. Furuno, T., Kanno, T., Arita, K., Asami, M., Utsumi, T., Doi, Y., Inoue, M., Utsumi, K., 2001. Roles of long chain fatty acids and carnitine in mitochondrial membrane permeability transition. *Biochem Pharmachol*, 68:1037-1046.
14. Tserevelakis, G. et al., 2014. Label-Free Imaging of Lipid Depositions in *C. elegans* Using Third-Harmonic Generation Microscopy. *PLoS ONE*, 9:e84431.
15. Mari, M. et al., 2015. Imaging ectopic fat deposition in Caenorhabditis elegans muscles using nonlinear microscopy. *Microscopy research and technique*, 78:523-528.
16. Lakowski, B. & Hekimi, S., 1998. The genetics of caloric restriction in Caenorhabditis elegans. *Proceedings of National Academy of Sciences of the United States of America*, 95:13091-13096.
17. Muzumdar, R. et al., 2008. Visceral adipose tissue modulates mammalian longevity. *Aging cell*, 7:438-440.
18. Huffman, D., M. & Barzilai, N., 2009. *Role of visceral adipose tissue in aging. Biochemica et biophysica acta*, 1970:1117-1123.
19. Settembre, C. et al., 2011. TFEB links autophagy to lysosomal biogenesis. *Science*, 332:1429-1433.
20. Cuervo, A., M., 2011. Cell biology. Autophagy's top chef. , *Science*, 332:1392-1393.
21. O'Rourke, E., J. & Ruvkun, G., 2013. MXL-3 and HLH-30 transcriptionally link lipolysis and autophagy to nutrient availability. *Nature cell biology*, 15:668-676.
22. Folick, A., et al., 2015. Aging. Lysosomal signaling molecules regulate longevity in Caenorhabditis elegans. *Science*, 347:83-86.